A Computational Study of the Ground and Excited State Structure and Absorption Spectra of Free-Base N-Confused Porphine and Free-Base N-Confused Tetraphenylporphyrin

Shubham Vyas,[†] Christopher M. Hadad,*[,†] and David A. Modarelli*[,‡]

Department of Chemistry, The Ohio State University, 100 West 18th Avenue, Columbus, Ohio 43210, and Department of Chemistry and The Center for Laser and Optical Spectroscopy, Knight Chemical Laboratory, The University of Akron, Akron, Ohio 44325-3601

Received: March 10, 2008; Revised Manuscript Received: May 12, 2008

Computational investigations into the ground and singlet excited-state structures and the experimental ground-state absorption spectra of N-confused tetraphenylporphyrin tautomers **1e** and **1i** and N-confused porphines (NCP) **2e** and **2i** have been performed. Structural data for the ground state, performed at the B3LYP/6-31G(d), B3LYP/6-31+G(d)//B3LYP/6-31G(d), and B3LYP/6-311+G(d)//B3LYP/6-31G(d) levels, are consistent with those performed at lower levels of theory. Calculations of the gas-phase, ground-state absorption spectrum are qualitatively consistent with condensed phase experiments for predicting the relative intensities of the Q(0,0) and Soret bands. Inclusion of implicit solvation in the calculations substantially improves the correlation of the energy of the Soret band with experiment for both tautomers (**1e**, 435 nm predicted, 442 nm observed in DMAc; **1i**, 435 nm predicted, 437 nm observed in CH_2Cl_2). The *x*- and *y*-polarized Q-band transitions were qualitatively reproduced for **1e** in both the gas phase and with solvation, although the low-energy absorption band in **1i** was predicted at substantially higher energy (646 nm in the gas phase and 655 nm with solvation) than observed experimentally (724 nm in CH_2Cl_2). Franck−Condon state and equilibrated singlet excited-state geometries were calculated for unsubstituted NCP tautomers **2e** and **2i** at the TD-B3LYP/SVP and TD-B3LYP/TZVP//TD-B3LYP/SVP levels. Electronic difference density plots were calculated from these geometries, thereby indicating the change of electron density in the singlet excited states. Adiabatic S_1 and S_2 geometries of these compounds were also calculated at the TD-B3LYP/SVP level, and the results indicate that while **2i** is a more stable ground-state molecule by ∼7.0 kcal mol^{-1}, the energy difference for the S_1 excited states is only ∼1.0 kcal mol^{-1} and is 6.1 kcal mol^{-1} for the S_2 excited states.

I. Introduction

The optical properties and photophysical behavior of porphyrins have been studied for quite some time and are reasonably well understood.[1,2] Research in this area has been quite useful in understanding the dynamics of light-induced processes in the light-harvesting complexes (LHCs) and photosynthetic reaction centers in purple bacteria and green plants.[3–5] The light-harvesting centers in green plants (LHCII)[3] and purple bacteria (LH2[4] and LH1)[5] are comprised of various bacteriochlorophyll *a* (BChl*a*) pigments arranged in circular arrays. Structural data indicate[6,7] that upon absorption of light, the efficient electronic energy transfer (EET) within LH1 and LH2 results from a combination of hopping and exciton coupling among the various BChl*a* pigments. Events within the photosynthetic reaction center (PRC) in these organisms then proceed when the electronically excited "special pair" of bacteriochlorophylls initiates photoinduced electron-transfer (ET), through a series of fast intermediate steps, to a quinone acceptor.[6] Bacteriochlorophylls are difficult to synthesize,[8,9] and as a result, solar energy conversion schemes mimicking the LHC and PRC have typically utilized porphyrins as energy and electron donors in covalently bound[10,11] and supramolecular multiporphyrin arrays.[12–14]

The optical properties[8,9] of bacteriochlorophylls and the related chlorins are substantially different from those of regular porphyrins, and more relevant (and readily synthesized) analogs of BChl*a* are therefore of considerable interest. N-confused porphyrins (NCPs) are attractive alternatives to porphyrins, chlorins, and bacteriochlorophylls in photonics applications because of their favorable optical properties and relatively facile synthesis, and they are therefore of increasing interest in the porphyrin community.[15] NCPs are porphyrin isomers having one of the pyrrolic nitrogens facing outside of the macrocycle and one C−H group oriented inward toward the core. While differing from the parent porphyrin by the inversion of only two atoms, these porphyrins exhibit significantly different physical and chemical properties than normal porphyrins. Two N-confused tetraphenylporphyrin (NCTPP) tautomers (**1e** and **1i** in Figure 1) are observed in solution.[16,17] One tautomer (**1e**) has an external N−H group and is favored in highly polar solvents such as DMF, presumably assisted by hydrogen bonding with the solvent.[16a] The second tautomer (**1i**) has two internal N−H groups and is the preferred tautomer in aromatic and halogenated solvents. The absorption spectra of both tautomers are characterized by Soret and Q-bands which are significantly red-shifted from, and with larger extinction coefficients than, tetraphenylporphyrin (H_2TPP).[16,17] The red-shifted absorption bands and increased oscillator strengths have been attributed[17] to a break in the degeneracy of the two sets of interacting orbitals (which are nearly degenerate in symmetric porphyrins) and that are commonly used to analyze porphyrin

* Corresponding authors. E-mail: (D.A.M.) dmodarelli@uakron.edu; (C.M.H.) hadad.1@osu.edu.

[†] Department of Chemistry, The Ohio State University.

[‡] Department of Chemistry and The Center for Laser and Optical Spectroscopy, Knight Chemical Laboratory, The University of Akron.

10.1021/jp802094r CCC: $40.75
Published on Web 07/01/2008

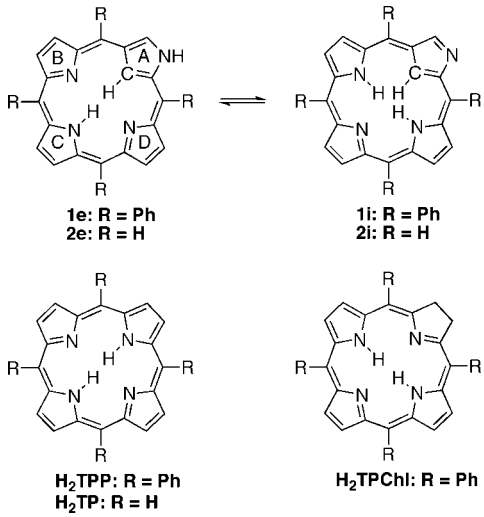

Figure 1. Tautomeric forms of N-confused tetraphenylporphyrins (**1e** and **1i**) and N-confused porphines (**2e** and **2i**). A, B, C, and D denote the nomenclature of the rings in the top left structure.

absorption spectra using the Gouterman four-electron, four-orbital model.[18]

Recently, we investigated the excited-state properties of NCPs **1e** and **1i** in solution using steady-state fluorescence and a combination of time-resolved fluorescence and absorption spectroscopies.[17,19] The results of these experiments were then interpreted in terms of the Gouterman four-electron, four-orbital model[18] using molecular orbitals obtained at the B3LYP/6-31G(d)//B3LYP/3-21G level of theory. For **1e**, the unoccupied a_2 and b_2 orbitals were found to split to higher and lower energies, respectively, relative to the analogous and nearly degenerate b_{1u} and a_u orbitals in H_2TPP, while the occupied a_2 orbital was found to increase substantially in energy relative to the occupied b_2 orbital. The atypical nature of the absorption spectrum of **1e** compared to a regular free-base porphyrin, with Q-band absorptions that increase in oscillator strength with decreasing energy, was interpreted within the context of those calculations to result from weakly allowed Q-band transitions. In tautomer **1i**, the degeneracy of the unoccupied a_2 and b_2 orbitals is also lifted, and the energy difference between the occupied a_2 and b_2 orbitals in **1i** becomes significant. The changes in orbital energies in **1i** are the opposite of what is observed in the reduced porphyrin tetraphenylchlorin (H_2TPChl), for which the unoccupied b_2 orbital increases in energy and the b_2 orbital decreases, while the occupied b_2 is higher in energy than the a_2 orbital. The net result of these changes are similar spectral characteristics for both **1i** and H_2TPChl, with the $Q_x(0,0)$ transition in **1i** becoming weakly allowed with a relatively large experimentally observed extinction coefficient.

In the current work, we sought to quantify this analysis using more precise computational methodologies, as well as to explain the observed transitions in the experimentally observed absorption spectra. Computational investigations of the electronic absorption spectra of regular porphyrins (and several derivatives) have included calculations ranging from semiempirical,[20] single and multireference (MR) configuration interaction (CI),[21] multiconfiguration second-order perturbation theory (CASPT2),[22] and time-dependent density functional theory (TD-DFT).[23] Excitation energies have also been calculated at the similarity transformed equation-of-motion coupled cluster and perturbation theoretical levels (STEOM-CC and STEOM-PT).[24] The less expensive TD-DFT has been shown to be in better agreement with experiment than the more expensive *ab initio* CI, CASPT2 or STEOM-CC calculations.[25] Herein we report a series of TD-DFT calculations, with application of the B3LYP functional,[26] on NCTPP tautomers **1e** and **1i** and unsubstituted NCP tautomers **2e** and **2i** in the gas phase as well as with consideration of implicit solvation via different solvent dielectric constants, in order to approximate the experimental solution-phase spectra and evaluate the absorption features of **1** and **2**. Electronic difference density plots were rendered in order to show the electronic changes which occur on excitation from the ground to the excited states. Furthermore, the Franck−Condon (FC) vertical excitation states of **2e** and **2i** were relaxed down along the S_1 and S_2 surfaces to obtain fully optimized excited-state geometries. Single-point TD-B3LYP/TZVP//TD-B3LYP/SVP calculations were also performed with all of the geometries to complete a potential energy surface of ground to excited-state excitation for the NCP tautomers, **2e** and **2i**.

II. Computational Methods

The ground-state geometries of NCTPPs (**1i** and **1e**) and NCPs (**2i** and **2e**) were optimized at the B3LYP/6-31G(d) level under C_1 symmetry using the Gaussian 03 software package.[27] All of these structures were confirmed to be minima via vibrational frequency analyses; zero-point vibrational energy corrections were not scaled. Single-point energy calculations at the B3LYP/6-31+G(d) and B3LYP/6-311+G(d) levels were performed to obtain more accurate energies with the B3LYP/6-31G(d) geometries. In order to approximate the experimental condensed phase and to evaluate the effect of different solvents, we utilized the polarizable continuum model (PCM)[28] implemented in Gaussian 03. Absorption spectra were then obtained at the B3LYP/6-31+G(d)//B3LYP/6-31G(d) level in both the gas and solution phases. Electronic difference density calculations were computed at the TD-B3LYP/SVP level using the ground-state optimized geometries at B3LYP/SVP level in the Turbomole-5.80 suite[29] of programs. To optimize the geometries of the singlet excited states at the TD-B3LYP/SVP level, the B3LYP/SVP optimized S_0 geometries were used as a starting point. The stationary points for the singlet excited states minima were confirmed by calculating the second derivatives by numerical evaluation of the analytical first derivative utilizing the NumForce module in Turbomole, thereby also providing the infrared (IR) spectra of the excited state. Using Turbomole, single-point energy calculations at the TD-B3LYP/TZVP//TD-B3LYP/SVP level were performed on all of these structures in the gas phase. Single-point energy calculations for considering the effect of implicit solvation (CH_3CN and CH_2Cl_2) were computed in Gaussian 03 at the TD-B3LYP/6-31+G(d) level of theory using the geometries optimized at the TD-B3LYP/SVP level of theory in Turbomole (see Supporting Information, Figure S16). The simulated spectra and plots of the density of states were obtained by using the GaussSum program.[30]

In comparing the theoretical and experimental work, we will designate the transitions yielding the experimentally observed bands as $S_0 \rightarrow$ A, B, C, etc., in order to distinguish between the computed transitions and the commonly referred to experimental transitions. Therefore, the transitions leading to the low energy $Q_y(0,0)$ and $Q_x(0,0)$ bands in the experimental spectrum, both of which are experimentally considered as arising from the $S_0 \rightarrow S_1$ transition but with different polarization, will be called the $S_0 \rightarrow$ A and $S_0 \rightarrow$ B transitions, respectively. Similarly, the transitions associated with the Soret or B-band will be called the $S_0 \rightarrow$ C transition and that of the N-band, the $S_0 \rightarrow$ D transition.

TABLE 1: Experimental and Calculated Absorption Data for Free-Base Porphine (H_2P) and Free-Base Tetraphenylporphyrin (H_2TPP)[a]

compound	Soret (nm)	Q-band (nm)			
		$Q_y(1,0)$	$Q_y(0,0)$	$Q_x(1,0)$	$Q_x(0,0)$
H_2P (expt)[b]	398 (1.4)	488 (0.237)	529 (0.025)	562 (0.064)	619 (0.0058)
H_2P (MRMP)[c]	400 (1.610)		486 (0.0143)		761 (0.0026)
H_2P (TD-DFT)[d]	379 (0.40)		519 (0.00004)		553 (0.00018)
H_2P (DFT/MRCI)[e]	404 (0.4846)		521 (0.0014)		639 (0.0007)
H_2P (TD-DFT)[f]	363, 372		508		544
H_2TPP (expt)[b]	418 (40.04)	514 (1.89)	548 (0.78)	590 (0.53)	648 (0.35)
H_2TPP (TD-DFT)[f]	378, 392		540		577

[a] The values in parentheses represent the calculated oscillator strengths and experimental extinction coefficients, shown as $\varepsilon \times 10^4$ M^{-1} cm^{-1}. [b] In benzene: Caughey, W. S.; Deal, R. M.; Weiss, C.; Gouterman, M. *J. Mol. Spectrosc.* **1965**, *16*, 415−427. Dorough, G. D.; Miller, J. R.; Huennekens, F. M. *J. Am. Chem. Soc.* **1951**, *73*, 4315−4320. Fonda, H. N.; Gilbert, J. V.; Coder, R. A.; Sprague, J. R.; Kamioka, K; Connolly, J. S. *J. Phys. Chem.* **1993**, *97*, 7024−7033. [c] Hashimoto, T.; Choe, Y.-K.; Nakano, H.; Hirao, K. *J. Phys. Chem. A* **1999**, *103*, 1894−1904. [d] Sundholm, D. *Phys. Chem. Chem. Phys.* **2000**, *2*, 2275−2281; Sundholm, D. *Chem. Phys. Lett.* **2000**, *317*, 392−399. [e] Parusel, A. B. J.; Grimme, S. *J. Porphyrins Phthalocyanines* **2001**, *5*, 225−232. [f] Zhang, Y.-H.; Ruan, W.-J.; Li, Z.-Y.; Wu, Y.; Zheng, J.-Y. *Chem. Phys.* **2005**, *315*, 201−213.

III. Results and Discussion

A. Geometry Optimizations. The ground-state geometries of NCPs (**1i**, **1e**, **2i** and **2e**) were optimized at the B3LYP/6-31G(d) level of theory under C_1 symmetry. The geometries of **1i** and **1e** are consistent with experiment[16b] and those calculated earlier,[17] with the N-confused A ring in **1i** (Figure 1) being significantly canted out of the macrocyclic plane. The distortion from planarity in this NCP results from the steric congestion caused by the presence of the extra hydrogen in the middle of the ring. In contrast, the geometry of the macrocycle in **1e** is largely planar. The phenyl rings in both compounds are twisted out of planarity, with dihedral angles (τ) ranging from 105 to 133° for **1i** and from 111 to 126° for **1e**, and the phenyl rings are oriented in a geared relationship. The calculated B3LYP/6-31G(d) relative energies of **1i** and **1e**, with **1i** being more stable than **1e** by 5.6 kcal mol^{-1}, are similar to those obtained at the B3LYP/6-31G(d)//B3LYP/3-21G(d) level,[17] for which **1i** was found to be more stable than **1e** by 5.5 kcal mol^{-1}. Single-point energy calculations using larger basis sets reduced this energetic preference for **1i** only slightly, to 4.9 kcal mol^{-1} at the B3LYP/6-31+G(d)//B3LYP/6-31G(d) level and 4.8 kcal mol^{-1} at the B3LYP/6-311+G(d)//B3LYP/6-31G(d) level. The preference for **1i** has been previously[17,31] attributed to the aromaticity of this tautomer, a feature that is not present in **1e** because of the break in conjugation of the A ring (Figure 1).

The geometries of NCPs **2i** and **2e** are comparable to those reported earlier[31] and also those of **1i** and **1e**, except that distortion of the NCP macrocycle in the internally protonated tautomer occurs only at the A ring in **2i**. There are negligible deviations in geometrical parameters relative to previous studies as there were no constraints applied in the current geometry optimizations. The geometry of tautomer **2e** is largely planar, similar to that of **1e**. The difference in the relative energies of NCPs **2i** and **2e** is greater than observed in the two NCTPP tautomers, where the energy difference is smaller because of the partial aromatic stabilization that results from the presence of the four phenyl groups in **1e**. Thus, tautomer **2i** is more stable than internally protonated tautomer **2e** by 9.0 kcal mol^{-1} at the B3LYP/6-31G(d) level. This energy difference was reduced to 6.9 kcal mol^{-1} with single-point energy calculations at the B3LYP/6-31+G(d)//B3LYP/6-31G(d) and B3LYP/6-311+G(d)//B3LYP/6-31G(d) levels of theory. This value is slightly higher than those reported by Ghosh et al.[31] using the VWN local exchange-correlation functional in conjunction with Perdew−Wang nonlocal corrections, in which **2i** was found to be more stable by 5.7 kcal mol^{-1}. This discrepancy is attributed to their assumption of planarity for these NCPs, rather than C_1 symmetry in our computations.

B. Electronic Absorption Calculations and Comparison with Experimental Spectra. In order to understand the predicted absorption spectrum of NCPs (**1i**, **1e**, **2i**, and **2e**), it is first instructive to review the experimental spectra of the analogous regular porphyrins (Figure 1), i.e., free base porphine (H_2P) and free base tetraphenylporphyrin (H_2TPP). The absorption spectra of free-base porphyrins are characterized by two distinct sets of absorption bands: (1) the low energy $S_0 \rightarrow S_1$ transitions (Q-bands) that are nearly forbidden by parity rules as a result of the high D_{2h} symmetry (D_{4h} symmetry in metalloporphyrins), and (2) the more intense, higher energy allowed $S_0 \rightarrow S_2$ transition called the Soret or B-band. In the highly descriptive Gouterman four-orbital, four-electron model,[18] the Q-band transitions are composed of linear combinations of the $b_{1u}-b_{2g}/a_u-b_{3g}$ (Q_x) and $b_{1u}-b_{3g}/a_u-b_{2g}$ (Q_y) transitions. The Q_x and Q_y transitions are traditionally assigned to the $1B_{3u}$ and $1B_{2u}$ electronic states, respectively.[32] In free base porphyrins (i.e., H_2TPP), each Q-band transition further splits by vibronic coupling, and is consequently observed as a pair of bands with each primary band, $Q_x(0,0)$ and $Q_y(0,0)$, having a higher energy ($Q_x(1,0)$ and $Q_y(1,0)$) vibrational overtone.

The Soret band, on the other hand, is an allowed transition that is comprised of a linear combination of the a_u-b_{3g} and $b_{1u}-b_{2g}$ transitions. This band has been assigned by multiple computational groups to a combination of the $2B_{2u}$ and $2B_{3u}$ states.[32f,33b,f] Experimentally, the intensity of this peak is significantly larger than those of the Q-band transitions, with extinction coefficients on the order of $\sim 5 \times 10^5$ M^{-1} cm^{-1} for the Soret band and $\sim(5-20) \times 10^4$ M^{-1} cm^{-1} for the Q-bands.

Substitution of the four phenyl rings at the *meso* positions of the porphyrin macrocycle has a marked effect on both the experimental and calculated absorption spectra. Experimentally,[33] the Q-bands are observed to red-shift significantly (Table 1), with the $Q_x(0,0)$ band shifting from 616 nm in H_2P to 648 nm in H_2TPP and the $Q_y(0,0)$ band shifting from 518 to 548 nm. The Soret band is likewise shifted, although not to such a great extent, occurring at 396 nm for H_2P and 418 nm for H_2TPP. Of the various computational methods employed to study H_2P, only one study (TD-B3LYP/6-31G(d)) has also been used to examine the absorption spectrum of H_2TPP.[34] In this work, although the absorption bands did not match exactly with experiment, the relative *shifts* in absorption as a function of

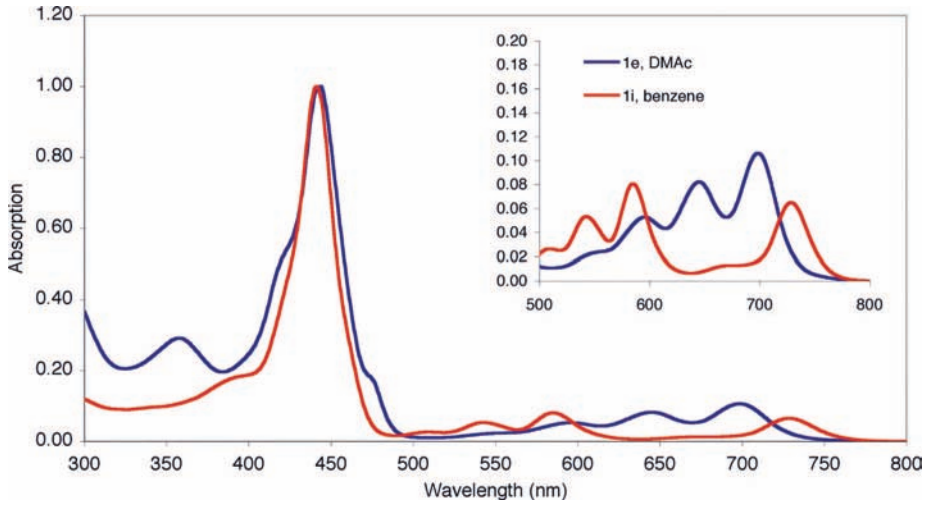

Figure 2. Experimental absorption spectra of **1i** (red) in benzene and **1e** (blue) in *N*,*N*-dimethylacetamide. The spectra are normalized for intensity of the Soret bands. The inset in the upper right shows an expanded view of the Q-band region. The N-bands in both solvents are at 350−380 nm, and the Soret bands are at at ∼440 nm.

meso phenyl substitution were shown to correlate very well. These data are important and indicate that the computed values of N-confused H_2P and N-confused H_2TPP should by analogy correlate with one another, and will be useful in predicting the absorption spectrum of the yet-to-be prepared NC−H_2P.

In BChl*a* and chlorins, the unoccupied a_2 and b_2 orbitals are nondegenerate and substantially split in energy as a result of the reduction in symmetry of the macrocycle. The accompanying energetic changes in the four Gouterman orbitals cause the b_1-c_2 and b_2-c_1 transition energies to become different, and together with the breakdown in parity rules from the changes in symmetry, lead to the Q_x transition gaining significantly in intensity.[17,19,35] The b_1-c_1 and b_2-c_2 transition energies that comprise the Q_y transition, on the other hand, remain nearly equivalent, and this transition does not appreciably change in intensity. Several groups have investigated chlorin to computationally reproduce the effect that reduction of one pyrrole ring has on the computed absorption spectrum. The lower energy Q_x band was shown using MRMP theory to have a larger oscillator strength of 0.0215 at 700 nm and the Q_y 0.0001 at 512 nm, and 0.7938 at 389 nm in the Soret region,[33d] whereas calculations at the DFT-MRCI level shifted the energies of the Q_x (626 nm with an oscillator strength of 0.10) and Q_y bands (541 nm, 0.06), with the Soret band occurring at 390 nm (0.96).[33a]

The absorption spectra of the different NCP tautomers are distinctly different from one another, a property that appears to be solvent dependent and one that might be exploited for use in situations where a specific absorption band might be readily turned on or off. These spectra have been previously interpreted[19] (qualitatively) in terms of the Gouterman four-electron, four-orbital model.[18] The experimental absorption spectra of tautomers **1i** (in benzene) and **1e** (in *N*,*N*-dimethylacetamide, DMAc) are shown in Figure 2. In order to explore the origins of the transitions present in the absorption spectra of **1i** and **1e**, as well as to predict the absorption spectra for **2i** and **2e**, we performed calculations using time-dependent density functional theory (TD-DFT)[36] at the TD-B3LYP/6-31+G(d)//B3LYP/6-31G(d) level. All of the molecules under investigation have C_1 symmetry and therefore all of the states formally belong to representation A. In order to be consistent with the porphyrin literature for D_{2h} symmetry, we have assigned approximate symmetries to the states upon analysis of the orbitals involved in the transition. For some of the states, contributions of the different orbital-to-orbital transitions are too equivalent to assign one irreducible representation to that particular state; hence, they are attributed to a linear combination of multiple irreducible representations.

The simulated absorption spectrum (Figure 3) for **1i**, was constructed using the oscillator strengths calculated at the TD-B3LYP/6-31+G(d)//B3LYP/6-31G(d) level of theory, fitted to a Gaussian distribution with a full-width at half-maximum (fwhm) of 1500 cm^{-1}. The intensities of each band are reported relative to the largest peak in the Soret band region of the spectrum (i.e., 400−440 nm). Two bands are observed in the low-energy Q-band region of the calculated absorption spectrum. Computationally, the lowest energy Q-band occurs at ∼646 nm, with a second higher energy band having similar intensity centered at ∼581 nm. These bands correspond to transitions arising from $S_0 \rightarrow S_1$ ($1B_{2u}$) and $S_0 \rightarrow S_2$ ($1B_{3u}$) excitations, respectively, and are assigned to the $Q_y(0,0)$ and $Q_x(0,0)$ bands observed in the experimental spectra, respectively. The oscillator strengths calculated for **1i** are reasonably consistent with the experimentally determined extinction coefficients (Table 2). The vibrational structure of the excited-state surface cannot be determined with these calculations of the vertical excitations, and as a result, the vibronic overtones of the Q-bands will not be discussed.

A series of much more intense transitions are observed in the Soret band region which, when fit using the Gaussian broadening function, correspond to a large band centered at ∼405 nm with a relatively large shoulder at ∼420 nm. The bands at 405 and 420 nm are attributed to $S_0 \rightarrow S_4$ ($2B_{3u}$) and $S_0 \rightarrow S_3$ ($B_{1g} + B_{2u}$) excitations, respectively. A smaller cluster of transitions are observed in the 330−370 nm range and, when fit, appear to be analogous to the N-band observed in the experimental spectrum. The band maximum for the calculated Soret band transition is significantly blue-shifted from the experimental value of 437 nm, a fact that can be attributed to the lack of solvation in the gas-phase calculation. The experimental absorption spectra of NCPs are known to be solvent dependent,[16b,17,19] and in order to account for this dependency, we performed calculations using the PCM model and the dielectric constant (ε) for CH_2Cl_2 ($\varepsilon \sim 8.9$). The calculated spectrum is shown in Figure 3, and indicates a significant red-shift for the Soret transition from ∼405 to ∼425 nm. The Q-band and N-band transitions were also observed to shift toward the red, to 584 nm for the $Q_x(0,0)$ band and 655 nm for the $Q_y(0,0)$ band, and from 350 to 361 nm for the N-band. The

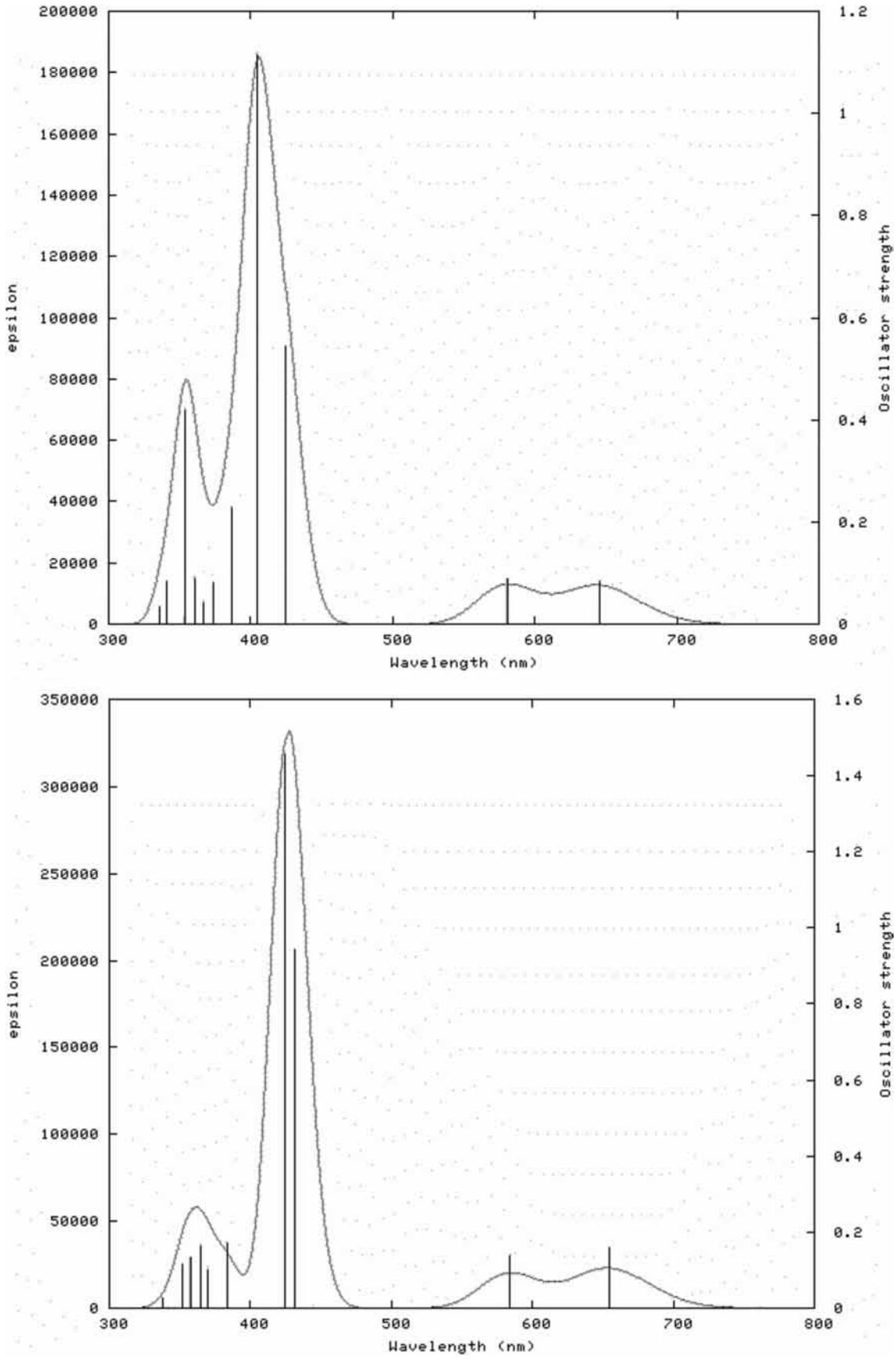

Figure 3. Simulated absorption spectra of **1i** in the gas phase (top) and using a dielectric continuum of $\varepsilon \sim 8.9$ (bottom) to simulate solvation by CH_2Cl_2. The calculated bands and oscillator strengths are shown as lines from the TD-B3LYP/6-31+G(d)//B3LYP/6-31G(d) calculations, and the overall spectrum was obtained by fitting those lines to a Gaussian distribution with a full width at half-maximum of 1500 cm^{-1}.

TABLE 2: Experimental and Calculated Absorption Data for N-Confused Tetraphenylporphyrin Tautomers 1e and 1i

compound	solvent	Soret (nm) ($\varepsilon \times 10^4$ M^{-1} cm^{-1})	Q-band (nm) ($\varepsilon \times 10^3$ M^{-1} cm^{-1})			
1i (expt)[a]	CH_2Cl_2	437 (15.9)	539 (7.8)	580 (10.8)	665 (2.7)	724 (10.4)
1i (calcd)[b,c]	CH_2Cl_2	424 (100)		584 (9.5)		655 (11)
1i (calcd)[b,d]	vacuum	405 (100)		581 (7.9)		646 (7.7)
1e (expt)[a]	DMAc	442 (11.9)	550 (2.0)	595 (6.1)	644 (9.5)	699 (12.4)
1e (calcd[b,e]	CH_3CN	426 (100)		575 (2.1)		686 (16)
1e (calcd)[b,e]	vacuum	415 (100)		579 (3.6)		702 (31)

[a] See refs 16 and 18. [b] Oscillator strengths are shown relative to the Soret band. [c] Calculated using the PCM model with $\varepsilon \sim 8.9$. [d] Calculated in the gas phase. [e] Calculated using the PCM model with $\varepsilon \sim 38$.

calculated oscillator strengths in the PCM calculation were also found to be more consistent with the experimentally determined extinction coefficients (Table 2).

Similar calculations were also performed on **1e** at the TD-B3LYP/6-31+G(d)//B3LYP/6-31G(d) level, and these results are shown in Figure 4 as simulated spectra calculated with the computed oscillator strengths and fitted to a Gaussian distribution with a fwhm of 1500 cm^{-1}. In the computed gas-phase spectrum, a prominent band is observed in the Q-band region at ~702 nm corresponding to the $Q_x(0,0)$ band, and with a relative oscillator strength of 31. A significantly smaller band (relative oscillator strength ~3.6) is observed at ~575 nm that corresponds to the $Q_y(0,0)$ band. These features correspond to transitions arising from $S_0 \rightarrow S_1$ ($1B_{2u}$) and $S_0 \rightarrow S_2$ ($1B_{3u}$) excitations, respectively. Two intense transitions and one weak transition were observed in the Soret band region, and these three calculated excitations contributed to the large transition centered at ~415 nm. This band is attributed to the $S_0 \rightarrow S_3$ ($B_{1u} + B_{2u}$), $S_0 \rightarrow S_4$ ($B_{1g} + B_{2u} + B_{3u}$), and $S_0 \rightarrow S_5$ ($1B_{1u}$) transitions. A series of smaller transitions, with similar intensity to the transition at 702 nm, are centered about 354 nm and are collectively attributed to the N-band absorption band. Consideration of implicit solvation using a PCM model with a dielectric constant similar to acetonitrile or nitromethane (i.e., $\varepsilon \sim 38$) results in a mild red-shift for the Soret band transition to ~426 nm, and a slight blue-shift for the low energy Q-band transitions to ~686 and ~575 nm. The N-band red-shifts from 354 to 363 nm upon solvation. The calculated oscillator strengths in both calculations, when scaled, are consistent with the experimentally determined extinction coefficients (Table 2).

The computed spectra are qualitatively similar to the experimental spectra with regard to the overall spectral shape and intensity pattern, particularly when fit to Gaussian distributions. A visual comparison between the Gaussian fits and the experimental spectra indicates that the computed spectra look remarkably similar to the experimental spectra without the vibronic overtones in the Q-band region. In general, the spectra calculated with consideration of the solvent's dielectric constant (ε) more accurately simulate the experimental spectra. Thus, the computed absorption maximum for the $Q_y(0,0)$ band of **1i** is blue-shifted 78 nm in the gas phase and 69 nm in the $\varepsilon \sim 8.9$ dielectric continuum (i.e., CH_2Cl_2). The $Q_x(0,0)$ band is red-shifted by 1−4 nm in the gas phase and in the solvent dielectric, while the Soret band is blue-shifted 32 nm (gas phase) and 12 nm (solvent dielectric). In the case of **1e**, the computed $Q_x(0,0)$ band is red-shifted 3 nm to the red in the gas phase (from 699 to 702 nm) and blue-shifted 13 nm in the solvent continuum. The computed $Q_y(0,0)$ bands are also blue-shifted, to 579 nm (gas phase) and 575 nm (solvent dielectric), from the experimental value of 595 nm. Finally, the Soret band positions in this tautomer are blue-shifted by 22 (gas phase) and 11 nm (solvent dielectric) from the experimental value (442 nm). It should be noted that although the qualitative aspects of the computed spectra are quite similar to the experimental spectra, the very low energy $Q_y(0,0)$ band at 724 nm observed in nonpolar solvents such as CH_2Cl_2 is not reproduced computationally. Thus, the S_1 energy of **1e** would appear to be lower than that of **1i**, a fact that is not experimentally observed. It is not clear at this time why this single anomaly exists.

A comparison of the ratios of the Soret band and Q-band extinction coefficients in the experimental spectra with the relative oscillator strengths in the computed spectra indicate that they are quite similar. The experimental spectra show a relative ratio of 100:12:8.2 for the Soret/Q_x/Q_y band extinction coefficients in **1i**, and a relative ratio of 100:18:6.8 for **1e**. In the computed spectra, the analogous ratios of the oscillator strengths using implicit solvation are 100:11:9.5 for **1i** and 100:16:2.1 for **1e**. With this information as a benchmark, we calculated the electronic structure and absorption spectra of the not-yet-synthesized NCP tautomers **2i** and **2e**.

The molecular orbitals of the NCTPPs **1i** and **1e** (Figure 5), obtained in this study as well as those reported previously,[17] are qualitatively similar to the orbitals for the NCP tautomers **2i** and **2e** (shown in Figure 6). In general, only the four frontier orbitals, LUMO+1 (b_{2g}), LUMO (b_{3g}), HOMO (b_{1u}), and HOMO-1 (a_u), are considered in the four-electron, four-orbital model. Since the ring system is no longer planar in the N-confused porphyrins, the previously degenerate LUMO and LUMO+1 orbitals in porphyrins (e_g symmetry, as designated in D_{4h}) are no longer degenerate. But the energetic ordering of these orbitals is not altered for the NCPs. Thus, if one approximates that the orbitals of **1** and **2** belong to the D_{4h} point group, then the frontier orbitals still maintain nominal e_g, e_g, b_{2u}, and a_{1u} symmetries, respectively. The differences, however, occur between NCTPP and NCP when orbitals from the HOMO-2 level and lower in the energetic manifold are considered. Specifically, in the case of NCTPPs, contributions from the π electrons of the phenyl ring are significant, and there are some differences in the orbital character deeper in the energetic manifold. Consequently, **1i** has HOMO-2 and HOMO-3 orbitals which are of b_{2g} symmetry, while **1e** instead has corresponding orbitals of b_{2u} and b_{3g} symmetry, respectively.

Similar to the computed spectra for **1i** and **1e**, the calculated spectra for NC−H_2P tautomers **2i** and **2e** were fitted to Gaussian distributions using a fwhm of 1500 cm^{-1} (Figures 7 and 8, respectively). The absorption bands in these spectra (Table 4) are significantly blue-shifted from NC−H_2TPP tautomers **1i** and **1e**, have less intense Q-band absorptions, and display a more pronounced solvent dependence. The computed $Q_y(0,0)$ band for **2i** in the gas phase is shifted 54 nm from that of **1i** to 592 nm. This band is assigned to the $S_0 \rightarrow S_1$ transition ($1B_{2u}$) and is less intense than the analogous computed band in **1i** by a factor of 4. The $Q_x(0,0)$ band, assigned to a $S_0 \rightarrow S_2$ transition ($1B_{3u}$), is predicted to absorb at 534 nm, blue-shifted 47 nm

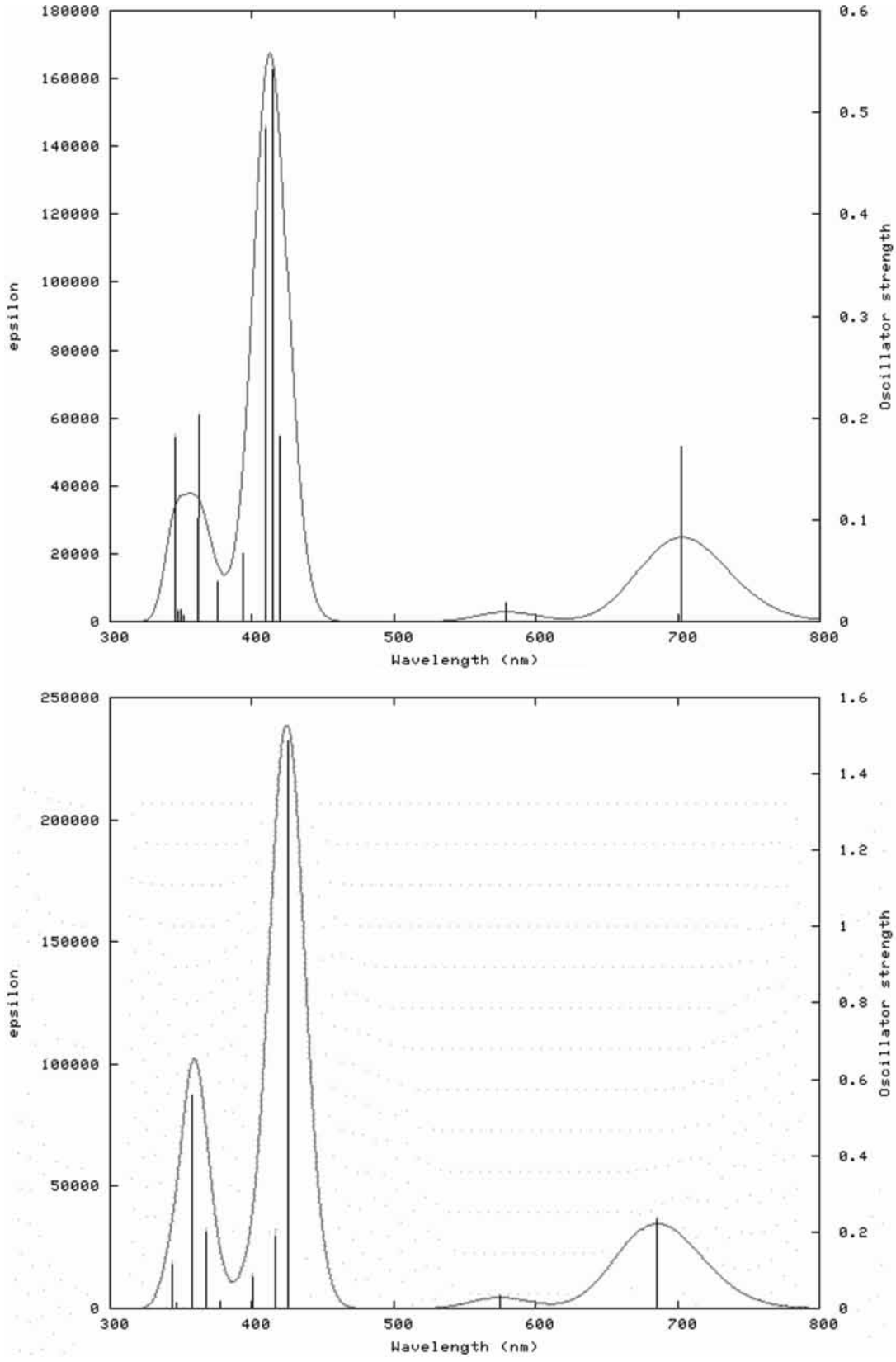

Figure 4. Simulated absorption spectra of **1e** in the gas phase (top) and a polar solvent (i.e., $\varepsilon \sim 38$ for acetonitrile or nitromethane) (bottom). The calculated bands and oscillator strengths are shown as lines from the TD-B3LYP/6-31+G(d)//B3LYP/6-31G(d) calculations, and the overall spectrum was obtained by fitting those lines to a Gaussian distribution with a full width at half-maximum of 1500 cm^{-1}.

from the computed $Q_y(0,0)$ band in **1i**. The $Q_y(0,0)$ band is also less intense by a factor of ~23 than the analogous band in **1i**, and is not visible in the simulated spectrum (Figure 7). A distinct and intense shoulder on the Soret band is observed at ~403 nm that is assigned to the $S_0 \rightarrow S_3$ ($B_{1g} + B_{2u}$) transition; a similar transition was also observed in the computed spectrum of **1i** and was assigned to the $S_0 \rightarrow S_3$ ($B_{1g} + B_{2u}$) transition, but was not resolved because of its energetic proximity to the

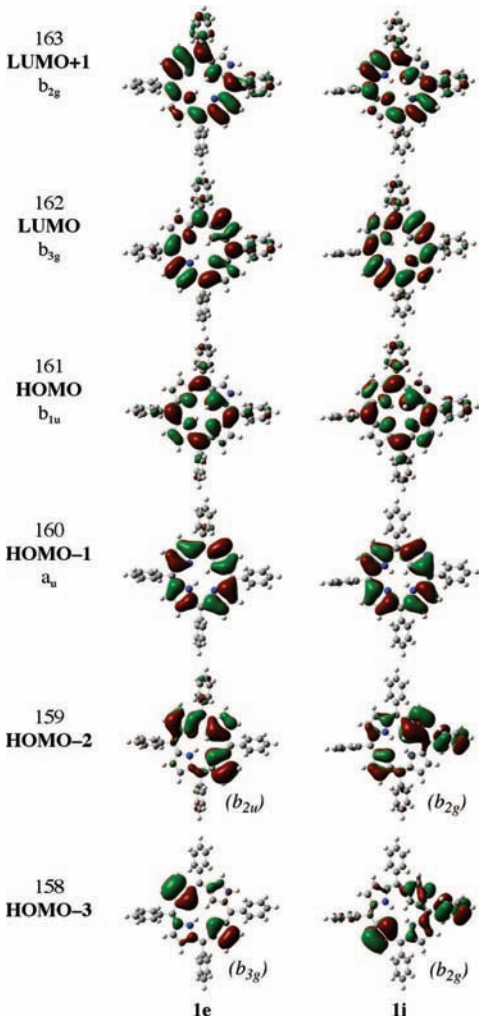

Figure 5. Molecular orbital plots of the NC-TPP tautomers at the B3LYP/6-31+G(d)//B3LYP/6-31G(d) level of theory in the gas phase.

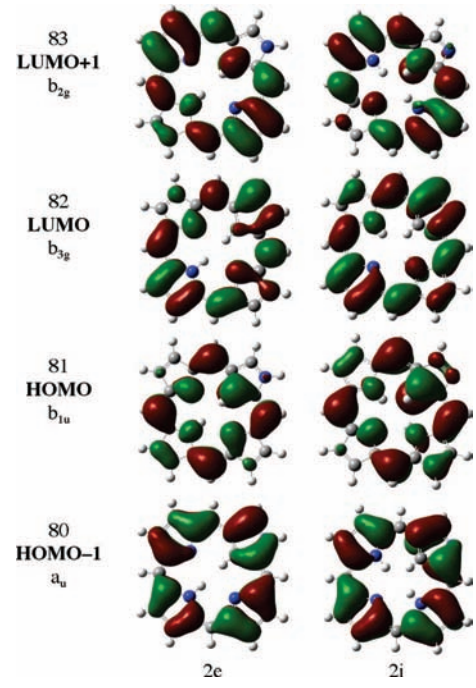

Figure 6. Molecular orbital plots of the NC−H_2P tautomers at the B3LYP/6-31+G(d)//B3LYP/6-31G(d) level of theory in the gas phase.

Soret band. The Soret band in **2i** is observed at ∼376 nm, and is assigned to the $S_0 \rightarrow S_4$ ($B_{1g} + B_{3u}$) transition. The characteristic N-band is observed at higher energy as a cluster of transitions at ∼320 nm, and in this spectrum, the ∼320 nm band is more intense than the Soret band.

Consideration of implicit solvation ($\varepsilon \sim 8.9$) using the PCM model for CH_2Cl_2 causes the entire spectrum to red-shift as the electronic states become compacted as a result of their interaction with the solvent's dielectric field. Both Q-bands are observed to be slightly red-shifted, while the Soret band is red-shifted by about 17 nm to a calculated peak at 394 nm. The $S_0 \rightarrow S_3$ transition that is observed as a low energy shoulder on the Soret band in the gas phase is no longer resolved, probably because of the pronounced shift in the Soret band. The N-band appears to have only moderate solvatochromism and is observed at the same energy as in the gas phase (∼320 nm), but with lower intensity. It is interesting to note that compared to the red shoulder at 402 nm in the gas phase, the Soret band has an extremely sensitive solvatochromic shift. This can be explained by the differences in the character of these states. The shoulder, i.e., the $S_0 \rightarrow S_3$ transition, has similar excitations contributing to it in the gas phase as well as in CH_2Cl_2. On the other hand, the Soret band consists of two transitions, $S_0 \rightarrow S_4$ and $S_0 \rightarrow S_5$. In the gas phase, these states have contributions from the *ungerade* symmetric transitions as well as the *gerade* symmetric transition (HOMO-2 to LUMO+1, B_{3g} symmetry); therefore, both of these states are partially allowed, have significant oscillator strength, and are close to each other. On the contrary, solvation renders the S_4 and S_5 states to have completely distinct symmetries, *ungerade* and *gerade* (HOMO-2 to LUMO+1, B_{3g} symmetry) respectively, making the transition to the S_4 state to be more allowed and conversely, the transition to the S_5 state is nearly forbidden. This solvation-induced difference is reflected in the ratio of the oscillator strengths of the $S_0 \rightarrow S_4$ and $S_0 \rightarrow S_5$ states, which is 2:1 in CH_2Cl_2 and is 11:1 in the gas phase. This separation of symmetries is a possible explanation as to why the Soret band appears to be more sensitive toward solvation than the shoulder, i.e., the $S_0 \rightarrow S_3$ transition.

The absorption bands for **2e** are similarly blue-shifted from those of **1e** in both the gas phase and the PCM calculations. The lowest energy band is observed at 653 nm in the gas phase, blue-shifted 49 nm from that of **1e**, and is attributed to the $Q_x(0,0)$ band. This band is again assigned to the $S_0 \rightarrow S_1$ transition ($1B_{2u}$) and is relatively more intense than the low energy band predicted for **2i**. Similar to **2i**, the $Q_y(0,0)$ band, assigned to the $S_0 \rightarrow S_2$ transition ($1B_{3u}$), is predicted to absorb at 533 nm and is again very weak. Unlike the $S_0 \rightarrow S_2$ transition in **2i**, this band is visible in the simulated spectrum. The distinct shoulder visible on the red edge of the Soret band in the gas-phase spectrum of **2i** is not apparent in **2e**, as the $S_0 \rightarrow S_4$ ($B_{2u} + B_{1g}$) transition is again close to the Soret band. The Soret band itself has a maximum at ∼370 nm in the gas phase, and is assigned to the $S_0 \rightarrow S_6$ ($A_g + B_{3u}$) transition. The N-band cluster of transitions is observed at ∼318 nm in this spectrum, with an oscillator strength that is 57% of the Soret band. The spectrum calculated using the PCM model with acetonitrile as the solvent shows the $Q_x(0,0)$ band is blue-shifted (i.e., ∼12 nm) when compared to the gas-phase spectrum. The $Q_x(0,0)$ band is observed at 623 nm while the $Q_y(0,0)$ band is weak and only barely visible at 530 nm. The Soret band is now dominated by the $S_0 \rightarrow S_4$ transition located at 392 nm, which is red-shifted by 18 nm from the gas-phase spectrum. This S_4 state at the PCM level is the same state as observed for S_6 in the gas phase,

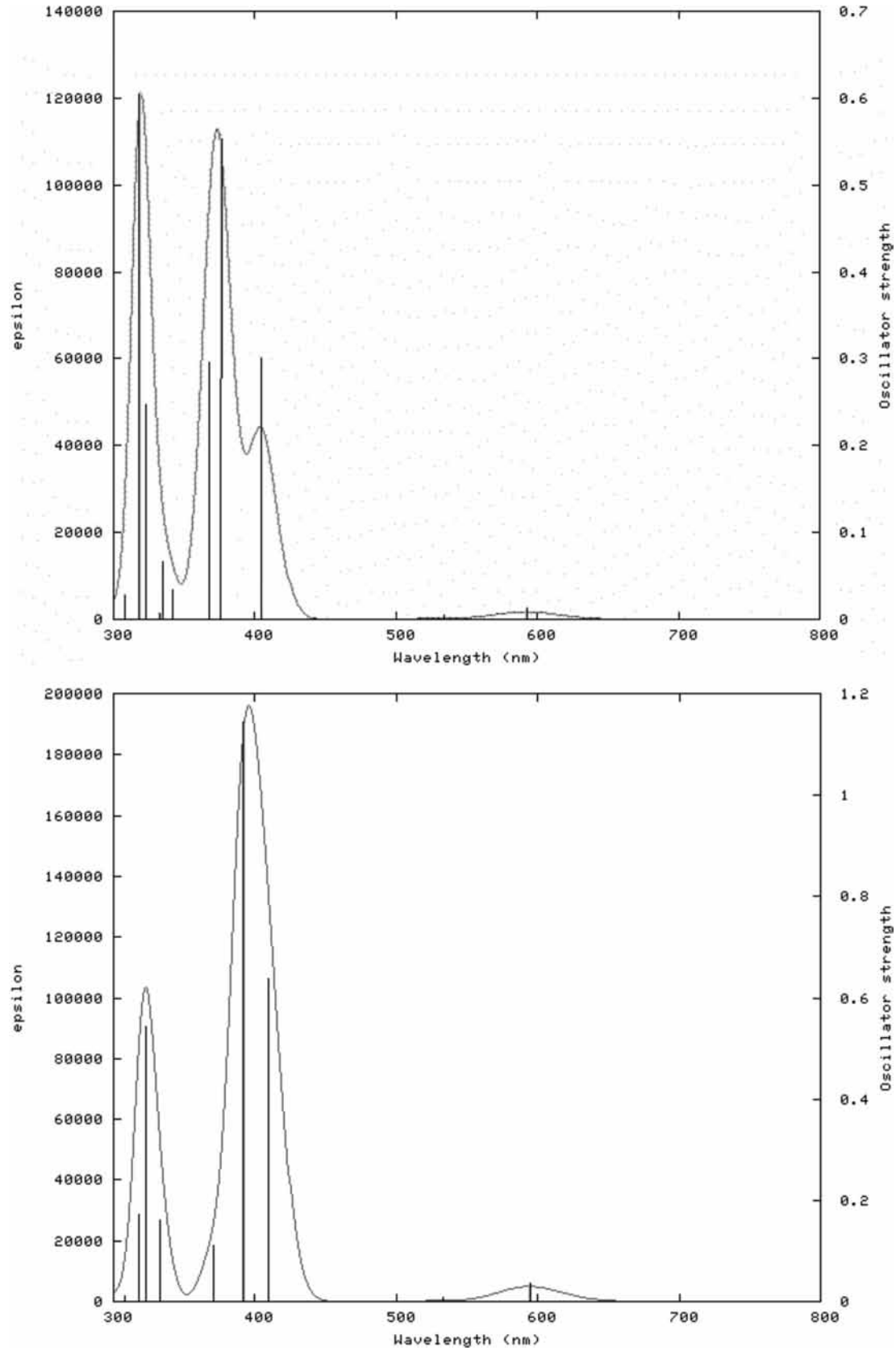

Figure 7. Simulated absorption spectra of **2i** in the (top) gas phase and (bottom) nonpolar solvent (i.e., CH_2Cl_2 ($\varepsilon \sim 8.9$)). The calculated bands and oscillator strengths are shown as lines from the TD-B3LYP/6-31+G(d)//B3LYP/6-31G(d) calculations, and the overall spectrum was obtained by fitting those lines to a Gaussian distribution with a full-width at half-maximum of 1500 cm^{-1}.

with both composed of a combination of A_g and B_{3u} symmetries. Finally, a small shoulder is observed on the red edge of the N-band, which is only slightly affected by the solvent's dielectric constant and is computed to occur at 321 nm.

The blue-shifted absorption bands in the unsubstituted NCPs **2e** and **2i** can be explained by the decreased density of states (DOS) of these tautomers relative to **1e** and **1i**, a graphical representation of which is shown as a function of orbital energy

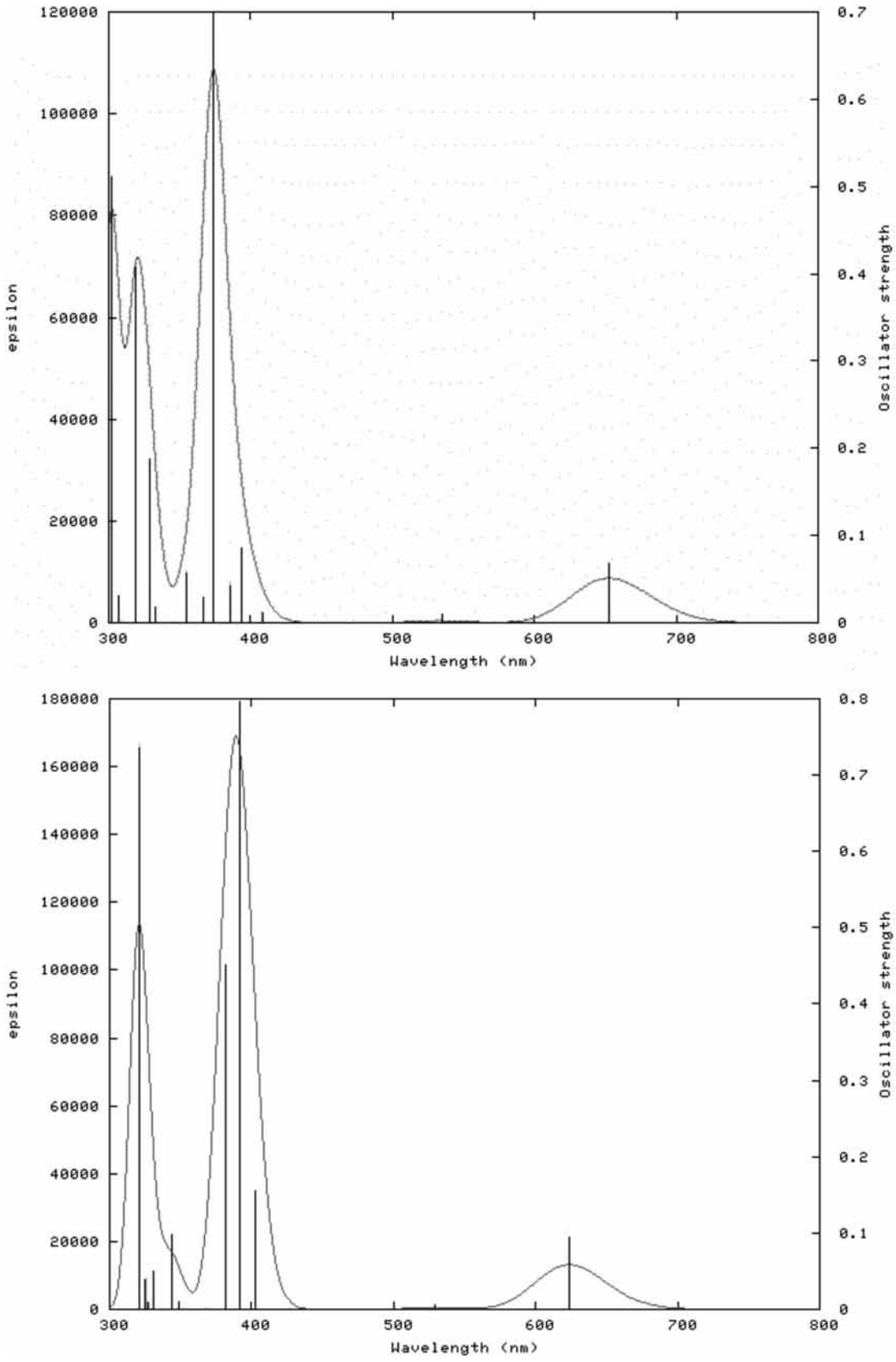

Figure 8. Simulated absorption spectra of **2e** in the (top) gas phase and (bottom) polar solvent (i.e., $\varepsilon \sim 38$ for acetonitrile or nitromethane) (bottom). The calculated bands and oscillator strengths are shown as lines from the TD-B3LYP/6-31+G(d)//B3LYP/6-31G(d) calculations, and the overall spectrum was obtained by fitting those lines to a Gaussian distribution with a full-width at half-maximum of 1500 cm^{-1}.

in Figure 9. In these plots, the green lines represent the occupied orbitals and the blue lines represent the virtual orbitals. In the virtual orbital space, the N-confused tetraphenyl derivatives (NC−H_2TPP, **1e** and **1i**) have ∼150% greater DOS than that of the two unsubstituted tautomers because of the presence of the four phenyl groups. The decreased DOS in **2i** and **2e** decreases the energy gap between the occupied and unoccupied orbitals and leads to the predicted blue-shifted absorption bands.

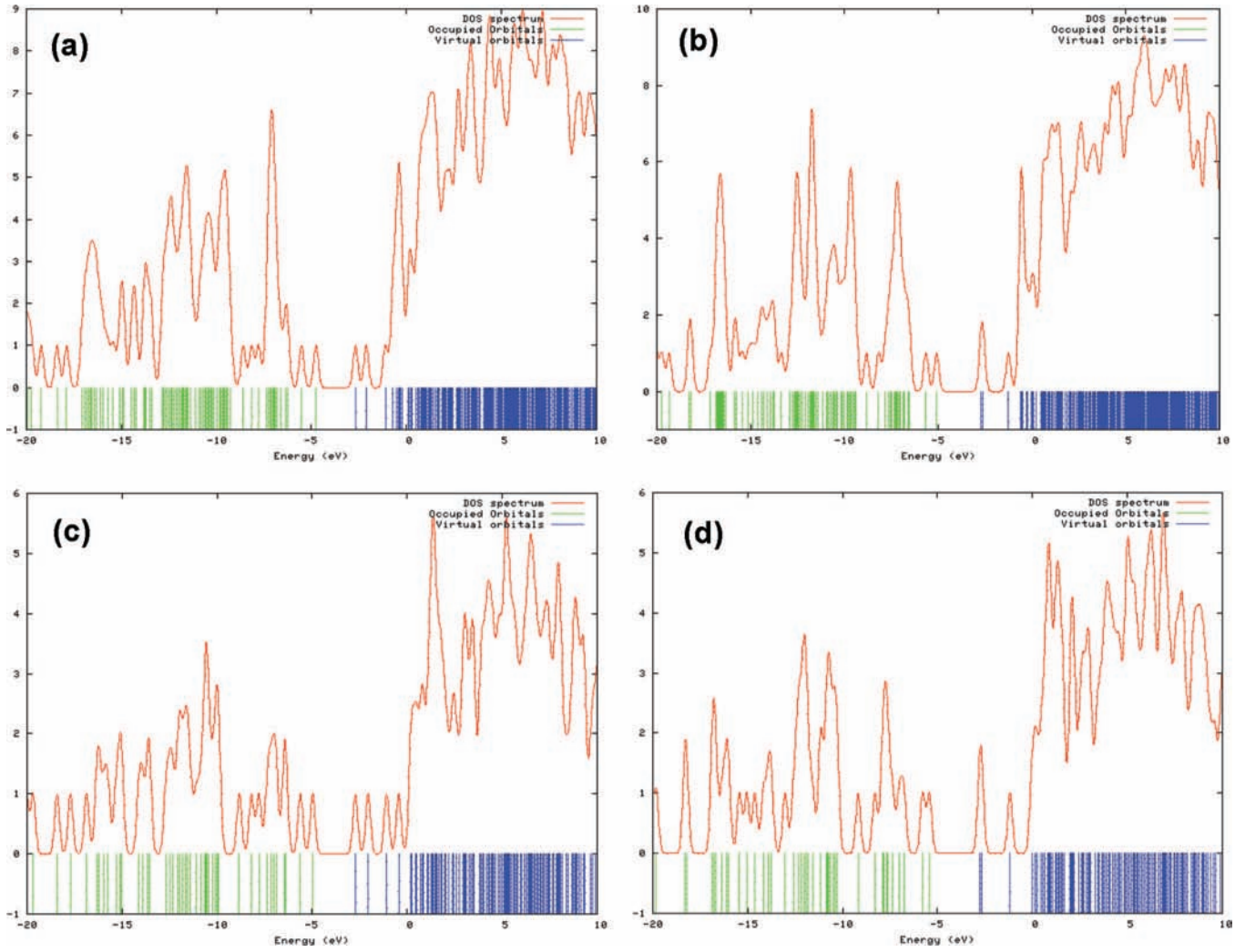

Figure 9. Density of states (DOS) for **1e** (a), **1i** (b), **2e** (c) and **2i** (d) plotted as a function of orbital energy (eV) at the B3LYP/6-31+G(d)//B3LYP/6-31G(d) level of theory in the gas phase. The green lines in the plots represent the occupied orbitals and the blue lines represent the unoccupied orbitals. The red line in each plot represents the distribution of the density of states as a function of orbital energy plotted using a fwhm of 0.3 eV.

In addition to the blue-shifted bands, NCP tautomers **2i** and **2e** have a distinctly weaker Q-band region than **1i** and **1e**. This can be explained by the energy gap between the four frontier orbitals which contribute to $Q_x(0,0)$ and $Q_y(0,0)$ bands. The intensity of the Q-bands is affected by the energy gap between these orbitals as linear combinations of the energy gaps determine the $Q_x(0,0)$ and $Q_y(0,0)$ bands, as explained by the Gouterman model.[18]

In general, the lower energy Q-band is a combination of HOMO to LUMO and HOMO-1 to LUMO+1 excitations (~10% contribution for **2e** and ~30% contribution for **2i**). The second Q-band is a combination of HOMO to LUMO+1 and HOMO-1 to LUMO transitions. The energy gap between the HOMO and LUMO orbitals is increased by about 4−6 kcal mol^{-1} in the case of **2** relative to **1**. The Q bands for the aromatic tautomers have comparable intensities, but the nonaromatic tautomers display a large difference between the intensities of the respective Q-bands. This observation is consistent with the experimental absorption spectra (Figure 2) and can also be addressed by the Gouterman model.[18] From Table 3, it is clear that LUMO and LUMO+1 are more degenerate for the aromatic tautomers (**1i** and **2i**), which results in iso-energetic linear combinations, yielding similar or relatively comparable intensities of the Q-bands.

TABLE 3: Relative Energies of the Four Frontier Orbitals at the B3LYP/6-31+G(d)//B3LYP/6-31G(d) Level in the Gas Phase and Using the PCM Model for Implicit Solvation (CH_3CN for 1e and 2e and CH_2Cl_2 for 1i and 2i)[a]

	orbital	1i	1e	2i	2e
gas phase	LUMO+1 (b_{2g})	70.4	78.5	71.8	82.2
	LUMO (b_{3g})	67.9	65.4	69.1	66.6
	HOMO (b_{1u})	13.1	17.5	8.1	15.0
	HOMO-1 (a_u)	0.0	0.0	0.0	0.0
PCM model	LUMO+1 (b_{2g})	71.2	78.1	71.6	79.8
	LUMO (b_{3g})	67.9	66.3	68.0	65.4
	HOMO (b_{1u})	13.8	16.8	7.8	15.2
	HOMO-1 (a_u)	0.0	0.0	0.0	0.0

[a] The energies of the orbitals are shown in kcal mol^{-1} with respect to the HOMO-1 orbital energy.

Although marked differences exist between the predicted spectra of **2i** and **2e** and of **1i** and **1e**, several characteristic features are nonetheless quite similar. For the internally protonated and aromatic tautomers **1i** and **2i**, the $S_0 \rightarrow S_3$ transitions are quite prominent and are resolved as shoulders on the red edge of the Soret band. In addition, the $S_0 \rightarrow S_4$ transition is the most intense transition and is mostly responsible for the Soret band. For the externally protonated tautomers **1e** and **2e**,

TABLE 4: Calculated Absorption Data (TD-B3LYP/6-31+G(d)//B3LYP/6-31G(d)) for N-Confused Porphine Tautomers 2e and 2i in the Gas Phase and at the PCM Level (i.e., CH_2Cl_2, and CH_3CN)

compound	solvent	N-band (nm) (oscillator strength)[a]	Soret (nm) (oscillator strength)[a]	Q-band (nm) (oscillator strength)[a]	
2i	CH_2Cl_2[b]	323 (48)	393 (100)	534 (0.17)	594 (3.0)
2i	vacuum[c]	318 (108)	376 (100)	533 (0.37)	592 (2.1)
2e	CH_3CN[d]	321 (93)	392 (100)	530 (0.52)	624 (11)
2e	vacuum[c]	318 (57)	374 (100)	533 (0.44)	653 (8.6)

[a] The reported oscillator strengths are relative to the Soret band. [b] Calculated using the PCM model with $\varepsilon \sim 8.9$. [c] Calculated in the gas phase. [d] Calculated using the PCM model with $\varepsilon \sim 38$.

the $S_0 \rightarrow S_3$ shoulder is of lower intensity and cannot be resolved as a shoulder or a separate peak.

C. Difference Density Calculations. When an electronic transition from the ground-state to the excited-state has multiconfigurational character, visualizing the electronic distribution by examination of the molecular orbitals involved in the transition can be nontrivial. Electronic difference density calculations represent a way to overcome this problem, for which one can subtract the ground-state electron density (S_0) from the Franck−Condon electron density of the excited state, thereby providing a picture of the redistribution of the electron density after the vertical transition from the ground-state to any of the Franck−Condon excited states. Visualization of these difference density plots allows one to more readily determine the changes to the electronic features on the excited-state surface, and can provide an insight into the subsequent geometric changes occurring on the excited-state potential energy surface. We have recently utilized this methodology to interpret several different photochemical problems,[37] but this approach has been used for a number of years.[38] In the work discussed here, we performed calculations using the TD-B3LYP methodology within Turbomole-5.80 to complete difference density calculations, after first reoptimizing the ground-state structures of **2e** and **2i** at the B3LYP/SVP level of theory. In these calculations, NCP **2i** is found to be stabilized by 7.3 kcal mol^{-1} relative to tautomer **2e**. This energy difference is in good agreement with the calculations performed at the B3LYP/6-311+G(d)//B3LYP/6-31G(d) level, 6.9 kcal mol^{-1}, as discussed above in section III.A.

The calculated difference density plots are depicted in Figure 10. In this figure, the green contours indicate where the electron density has moved to in the Franck−Condon singlet excited state, while the red contours show where the electron density has been depleted from the S_0 state. It is clear from this figure that the $S_0 \rightarrow S_1$ transition in **2i** mainly involves electronic changes in the N-confused A ring, as there is little change in the electron density on the other rings in the macrocycle. On the other hand, the change in electron density in the $S_0 \rightarrow S_1$ transition of **2e** is delocalized on the entire macrocycle. Comparing the amount of delocalization in the two tautomers gives an indirect indication of the relative stabilities of the S_1 state in each tautomer, wherein tautomer **2i** should have a higher energy S_1 state, relative to the corresponding S_0 state, than the more delocalized S_1 state of tautomer **2e**, compared to its corresponding S_0 state. This qualitative analysis is confirmed by comparison of the vertical excitation energies for the two transitions: 48.2 and 43.3 kcal mol^{-1} for **2i** and **2e**, respectively, at the TD-B3LYP/SVP level. The changes in electron density upon vertical excitation also provide information regarding subsequent geometric changes for the S_1 state. In other words, we can predict with some confidence that relaxation of the S_1 state of **2i** from its Franck−Condon state to its equilibrated excited-state geometry will require less distortion than the S_1 state of **2e**, as there appears to be less electron density movement upon S_1 excitation of **2i**.

Difference density plots corresponding to the S_2 state are also shown in Figure 10 with the same isocontour value to have a comparative view of both the states. It is clear that there is significantly more electron density movement in the $S_0 \rightarrow S_1$ transition relative to the $S_0 \rightarrow S_2$ transition. (Plots with lower iso-contour values corresponding to the S_2 state are in the Supporting Information, Figure S9). The tautomer **2i** has the transition localized again in the A ring, in particular at one of the internal C−C bonds, but tautomer **2e** has the transition comparatively delocalized on all of the rings and bridges. This observation is similar as was noted in the case of $S_0 \rightarrow S_1$ transition. In contrast to the discussion above in context of the $S_0 \rightarrow S_1$ transition, there is less reorganization of the electron density for the $S_0 \rightarrow S_2$ transition. This similarity is also reflected in the vertical excitation energies of the transition in both tautomers which are 53.7 and 53.5 kcal mol^{-1} for **2i** and **2e**, respectively. These plots also indicate that the S_2 state (the $S_0 \rightarrow$ B transition) will be more similar in character to the S_0 state rather than the S_1 state (the $S_0 \rightarrow$ A transition).

These plots also provide information about the significant change in the position of the $Q_x(0,0)$ band of **2e** upon solvation whereas all of the other Q-bands do not have prominent solvation effects as shown in Table 4. Since there is no appreciable electron density change over the entire macrocycle of the externally protonated tautomer **2i**, a pronounced effect of the solvent reaction field on the position of the $Q_x(0,0)$ and $Q_y(0,0)$ bands is not observed. Conversely, a significant electron density difference is observed for the $Q_x(0,0)$ band of **2e**, but not for the $Q_y(0,0)$ band; therefore, only the $Q_x(0,0)$ band has a significant energetic shift.

D. Optimization of the Excited States. In order to further characterize the excited-state potential energy surfaces for the two tautomers, both the S_1 and S_2 states of NCPs **2i** and **2e** were optimized at the TD-B3LYP/SVP level. After optimization, second derivatives were calculated numerically on the optimized geometries at the excited-state surfaces in order to confirm that each stationary point was a minimum on the respective potential energy surface. These frequencies represent the excited state's IR spectra and provide computed results with which to characterize transient IR experiments (see Supporting Information, Figures S10−S16). The optimized excited-state geometries, along with the optimized S_0 geometries and their corresponding geometric parameters, are shown in Figure 11. The illustrated bond lengths are the ones that changed by ±0.02 Å or more in the S_1 state when compared to the S_0 ground state.

Comparison of the optimized S_1 and S_0 states for each tautomer yields root-mean-square deviation (rmsd) values of 0.04_3 Å for **2i** and 0.05_3 Å for **2e**. These results indicate that the geometry of the S_1 state of **2i** is more similar than **2e** in geometry to its corresponding S_0 state, a conclusion that is in agreement with the qualitative discussion made earlier as determined by analyzing the difference density plots in Figure 10. The difference density plots indicated that upon $S_0 \rightarrow S_1$ excitation, the major changes in electron density for **2i** were

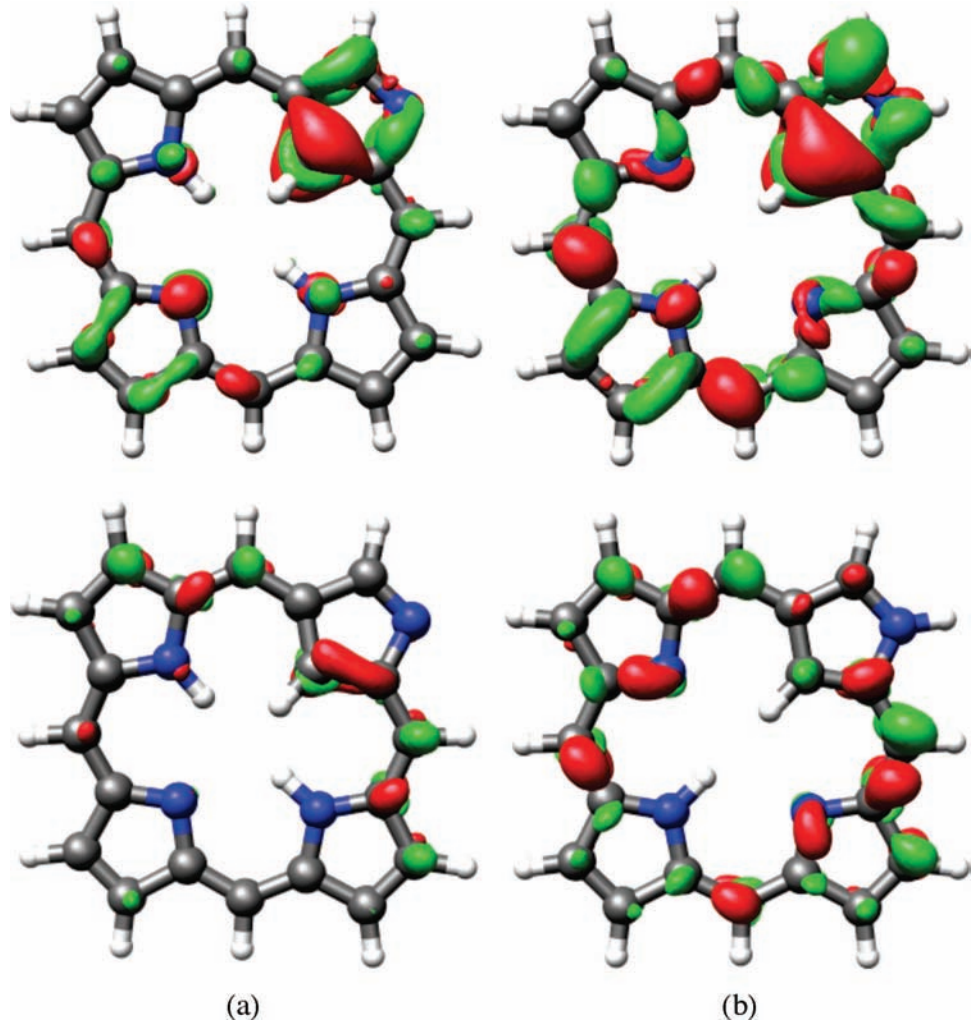

Figure 10. Electronic difference density plots for the S_1 state (top) and S_2 state (bottom) for (a) **2i** and (b) **2e** calculated at the TD-B3LYP/SVP level of theory. The green contours depict the accumulation of electron density in the excited state, and the red contours illustrate the loss of electron density from the S_0 ground state. The contour values are ±0.001 au. (The N-confused A ring is in the northeast corner of each plot.)

localized mainly on the A ring, and indeed, the largest bond length changes in the S_1 state are also located mainly on this ring. Thus, the internal C−C bonds on the A ring (C15−C18 and C17−C18) are elongated in the S_1 excited-state as electron density is depleted in these bonds, whereas the C16−C17 and C15−N4 bonds are contracted in the A ring as a result of the increase in electron density along those bonds in S_1. The external C−N double bond (C16−N4) is also elongated from 1.33 to 1.35 Å. Similar geometric changes, although less prominent, are also observed in the other three rings even though they were not obvious from the difference density plot.

For tautomer **2e**, the S_1 excited-state geometry of the entire macrocycle shows pronounced changes when compared to the ground-state geometry, again consistent with the difference density plot. Analogous to **2i**, the A ring has elongated internal C−C bonds (C2−C3 and C3−C5) and an elongated external C−N bond (C4−N12). Prominent changes also occur in the B and D rings, in which one internal C−N bond elongates and another one contracts, both changes of which are readily visualized in the difference density plots. The *meso*-pyrrole C−C bonds contract and elongate pairwise.

The two tautomers exhibit different modes of distortion relative to the macrocycle plane upon $S_0 \rightarrow S_1$ excitation. Tautomer **2i** becomes more distorted in the S_1 state, with H32 moving above the plane of the macrocycle while H25 and H27 move below the plane. In contrast, tautomer **2e** becomes more planar in S_1 with the out-of-plane hydrogen (H13) moving toward the plane of the macrocycle. These geometric distortions in the excited-state are consistent with the fact that, despite the small electron density changes for **2e** upon excitation, the rmsd value of 0.4_3 Å found for this tautomer is quite high.

After exploring the S_1 state ($S_0 \rightarrow A$), we investigated the S_2 state ($S_0 \rightarrow B$). Consistent with the difference density plots, we observed very minor changes in the optimized S_2 state geometries compared to the S_0 state geometries, indicating the S_2 states are more similar structurally in both cases to S_0 than to the S_1 states. The rmsd values for these structures relative to the corresponding ground states are 0.02_7 and 0.02_0 Å for tautomers **2i** and **2e**, respectively. For tautomer **2i**, the only noticeable change occurs at the internal C15−C18 bond of the A ring, which is elongated by 0.02 Å as predicted from the difference density plot. For externally protonated tautomer **2e**, the internal C−C bonds of ring B and D are changed significantly (∼±0.02 Å) as shown in Figure 11. Other less prominent changes occur at the C−C bonds connecting the *meso* carbons to the pyrrole rings, an effect that is also suggested by the difference density plots. Interestingly, there is almost no change in the planarity of the macrocycle for **2e** in S_2, while hydrogens H32, H27, and H25 all become more planar for the internally protonated tautomer **2i**. Because of this angular

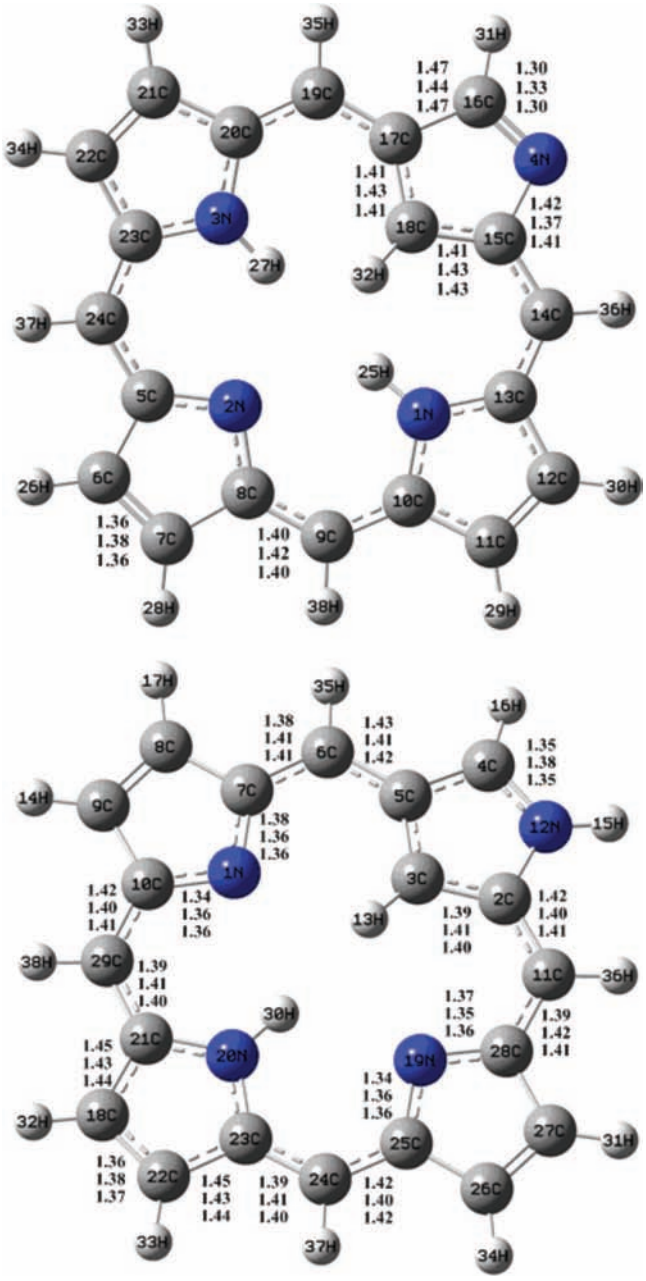

Figure 11. Optimized (TD-B3LYP/SVP) geometries of **2i** (top) and, **2e** (bottom). Selected bond lengths are in angstroms (Å). The top number corresponds to the S_0 state, the middle number corresponds to the S_1 state, and the bottom number corresponds to the S_2 state. All of the selected bond lengths have more than 0.01Å change in one of the excited states when compared to the ground state.

distortion, tautomer **2i** has a higher rmsd value than tautomer **2e** even though there are more significant bond length changes in **2e**.

Several points become apparent when comparing the S_0 ground-state and S_1 and S_2 excited-state geometries in **2i** and **2e**. For **2i**, the S_2 state is intermediate in structure between the S_0 and S_1 state structures, although both excited-state structures are distorted from the ground state. In addition, the excitation in both states is localized on the A ring. In contrast, the S_0 ground-state and S_2 excited-state of **2e** are structurally similar, while the S_1 geometry is different. Both excited-state structures for **2e** do indicate movement of electron density over the whole NCP skeleton.

E. Energetics. Combining the TD-B3LYP/SVP results for the ground states' optimizations, vertical excitations and singlet excited states' optimizations, ground and excited-state potential energy surfaces for **2i** and **2e** were then constructed (Figure 12). (We caution the reader, however, that there are many geometric differences between the respective surfaces, and it is difficult to render these details in a two-dimensional plot.) At this level of theory, the ground-state of **2i** is lower in energy than **2e** by 7.3 kcal mol^{-1}, probably because of the resonance stabilization afforded to the former tautomer. Vertical excitation of each tautomer produces the Franck−Condon excited singlet state. The energy of this excitation is 48.2 kcal mol^{-1} for **2i** and 43.3 kcal mol^{-1} for **2e**, and leads to Franck−Condon states that are 48.2 and 50.6 kcal mol^{-1} higher in energy than the **2i** ground state. Relaxation on the S_1 surface proceeds for **2i** with a relatively small structural change to an energy only 1.8 kcal mol^{-1} below the Franck−Condon state, while NCP **2e** undergoes a larger structural reorganization and upon relaxation is 3.8 kcal mol^{-1} below the Franck−Condon state. The net result of these changes is that the equilibrated S_1 excited state of NCP **2i** is lower in energy than the corresponding excited state of **2e** by ∼0.5 kcal mol^{-1}, indicating that the relaxed S_1 states are almost isoenergetic when compared to the energy difference of ∼7.3 kcal mol^{-1} in the ground state. These results correlate well with the energy of the computed low energy Q-band absorption, for which we calculate a lower energy transition in **2e** in both the gas and condensed phases.

The $S_0 \rightarrow S_2$ vertical transitions are at 53.7 and 53.5 kcal mol^{-1} for **2i** and **2e**, respectively. Relaxation of the Franck−Condon S_2 state to the geometrical minimum on the S_2 surface proceeds with a very small amount of relaxation energy when compared to the $S_0 \rightarrow S_1$ transition. The equilibrated S_2 state minima for **2i** and **2e** are located 0.4 and 1.5 kcal mol^{-1} lower than the corresponding Franck−Condon S_2 states, respectively. These values are about 5-fold and 3-fold smaller than the corresponding S_1 state energies of the **2i** and **2e** tautomers, respectively. Tautomer **2e** has a larger amount of relaxation energy, again consistent with the greater amount of change in the electron density observed in the difference density plots. Unlike the nearly isoenergetic relaxed geometries on the S_1 surface, both the Franck−Condon and relaxed geometries on the S_2 surface are quite different from one another. The energetic difference between **2i** and **2e** is consistent with that observed on the ground-state surface, since the vertical exctation energy for each $S_0 \rightarrow S_2$ transition is nearly identical. To check the accuracy of these calculations, we performed single-point energy calculations at the TD-B3LYP/TZVP//TD-B3LYP/SVP level of theory (also shown in Figure 12). Additional calculations were also performed at the TD-B3LYP/6-31+G(d) level of theory in Gaussian 03 using the geometries obtained from Turbomole, in order to compare energetics in the gas phase and in solution (see Supporting Information, Figure S16). These supplementary calculations also predicted that only the Franck−Condon S_1 state and the equilibrated S_1 state of the externally protonated tautomer **2e** are sensitive to solvation and undergo solvent-induced changes in energy. Indeed, all of the other excited states are not affected by solvation.

With this information, it is interesting to posit as to whether the data from **2i** and **2e** can be extrapolated to the experimentally observed photophysical properties of **1i** and **1e**. Unfortunately, the answer to this question is complex. The energetics of the S_1 state of **2i** and **2e**, similar to the computed absorption spectra **1i/2i** and **1e/2e**, indicate that the relaxed excited-state of **1i/2i** is lower in energy than **1e/2e**. This result indicates that the Q(0,0) band in the fluorescence spectrum of **1i** should be lower in energy than **1e** with an energy difference between the two

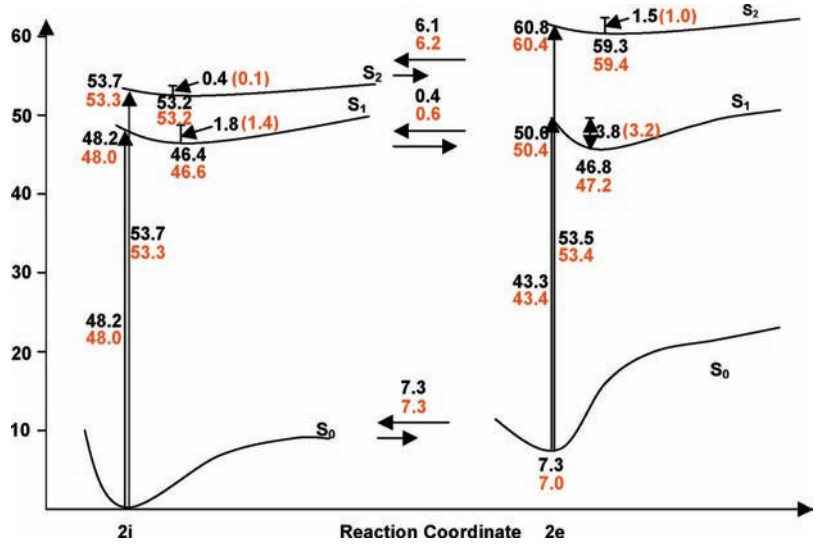

Figure 12. Gas-phase energetics (kcal mol^{-1}) obtained at the TD-B3LYP/SVP (black) and TD-B3LYP/TZVP//TD-B3LYP/SVP (red) levels for the ground and excited-state potential energy surfaces of **2i** and **2e**.

of about ~1.0 kcal mol^{-1}, which is in complete agreement with the observed results (i.e., $\lambda_{Q(0,0)}$ ~744 nm for **1i** and 713 nm for **1e** with ΔE ~1.6 kcal mol^{-1}). Additionally, the smaller amplitude of structural displacement upon relaxation from the initially prepared Franck−Condon state argues that **1i** should have a shorter excited-state lifetime and lower fluorescence quantum yield as a result of more rapid internal conversion, and this conclusion is also experimentally observed. From this discussion, it is clear that calculations on truncated NCPs **2** correlate well with the experiments performed on **1**. Nonetheless, future calculations on the significantly larger NC−H_2TPP tautomers may reveal the role of the attached phenyl rings in the dynamics of the excited states.

IV. Conclusions

In this work, we have computationally investigated the ground and singlet excited-state structures of two N-confused porphyrins, (1) the N-confused tetraphenylporphyrin tautomers **1i** and **1e** (NC−H_2TPP) and (2) the unsubstituted analogs **2i** and **2e** (NC−H_2P). The absorption features for both sets of tautomers were computed in both the gas phase and with consideration of implicit solvation and the solvent dielectric constant with the PCM model. We observe good qualitative agreement between the computed spectra and the experimental spectra for **1i** and **1e**. The Soret and Q-band regions are consistent with experiment in terms of the relative band shapes, although the low energy $Q_y(0,0)$ band is calculated to be higher in energy than is observed experimentally. The computed absorption spectra of **2i** and **2e** are similar to **1i** and **1e**. However, two differences between the spectra of the two sets of tautomers are notable: (a) for **2i** and **2e**, the Q-band region is greatly diminished in intensity compared to **1i** and **1e**, and (b) a significant blue-shift is observed for all bands, similar to what is observed for porphine and tetraphenylporphyrin. These blue-shifted spectra are attributed to the larger density of states in the *meso*-phenyl substituted NCPs **1i** and **1e** (as shown in Figure 9).

The excited-state geometries of **2i** and **2e** were optimized at the TD-B3LYP/SVP level in order to determine the correct energetic ordering in the ground and excited states, and, through extrapolation, begin to understand the excited-state dynamics experimentally observed for **1i** and **1e**. These calculations indicate that **2e** undergoes a more correlated set of bond changes upon relaxation from the initially prepared Franck−Condon state than **2i**, whose changes are largely limited to out-of-plane distortion of and changes in bond lengths for the N-confused A ring. Furthermore, the S_1 state is geometrically quite different than the S_0 state; whereas, the S_2 state is similar to the S_0 state.

Future computational work will include calculations of the Soret states, in order to gain insight into the nature of the experimentally observed $S_1 \rightarrow S_n$ transient absorption spectra. Calculations to examine the excited-state solvent dependence are also underway and will be reported in due course.

Acknowledgment. D.A.M. acknowledges the University of Akron for the support of this work. C.M.H. acknowledges financial support from the National Science Foundation and the National Institutes of Health. Generous computational resources from the Ohio Supercomputer Center are also gratefully acknowledged.

Supporting Information Available: Tables of Cartesian coordinates and energies for all computed structures and figures showing simulated absorption spectra for **1** and **2** with alternate fitting functions, difference density plots for the S_2 state of **2i** and **2e**, calculated IR spectra for the S_0, S_1 and S_2 states of **2i** and **2e**, and gas and solution phase energetics for the ground and excited state surface of **2i** and **2e**. This material is available free of charge via the Internet at http://pubs.acs.org.

References and Notes

(1) See: *The Porphyrin Handbook*; Kadish, K. M., Smith, K. M., Guilard, R., Eds.; Academic Press: San Diego, CA, 2000.

(2) (a) Gouterman, M. J. In *The Porphyrins*; Dolphin, D., Ed.; Academic Press: New York, 1978; Vol. III, pp 1−165. (b) Seybold, P. G.; Gouterman, M. *J. Mol. Spectrosc.* **1969**, *31*, 1–13.

(3) Kühlbrandt, W.; Wang, D. N.; Fujiyoshi, Y. *Nature* **1994**, *367*, 614.

(4) McDermott, G.; Prince, S. M.; Freer, A. A.; Hawthornthwaite-Lawless, A. M.; Papiz, M. Z.; Cogdell, R. J.; Isaacs, N. W. *Nature* **1995**, *374*, 517.

(5) Karrasch, S.; Bullough, P. A.; Ghosh, R. *EMBO J.* **1995**, *14*, 631.

(6) (a) For recent reviews of the events occurring in the photosynthetic reaction center and light-harvesting complex, see: Arnett, D. C.; Moser, C. C.; Dutton, P. L.; Scherer, N. F. *J. Phys. Chem. B* **1999**, *103*, 2014–2032. (b) Pullerits, T.; Sundström, V. *Acc. Chem. Res.* **1996**, *29*, 381–389.

(7) Amerongen, H. v.; Grondell, R. v. *J. Phys. Chem. B* **2001**, *105*, 604–617.

(8) (a) Strachan, J.-P.; O'Shea, D. F.; Balasubramanian, T.; Lindsey, J. S. *J. Org. Chem.* **2000**, *65*, 3160–3172. (b) Pandey, R. K.; Zheng, G. In *The Porphyrin Handbook*; Kadish, K. M., Smith, K. M., Guilard, R., Eds.; Academic Press: San Diego, CA, 2000; *Vol. 6*; pp 157−230. (c) Montforts, F.-P.; Gerlach, B.; Höper, F. *Chem. Rev.* **1994**, *94*, 327–347. (d) Smith K. M. In *Chlorophylls*; Scheer, H., Ed.; CRC Press: Boca Raton, FL, 1991; pp 115−143. (e) Taniguchi, M.; Ra, D. Y.; Mo, G.; Balasubramanian, T.; Lindsey, J. S. *J. Org. Chem.* **2001**, *66*, 7342–7354.

(9) (a) Hindin, E.; Kirmaier, C.; Diers, J. R.; Tomizaki, K. Y.; Taniguchi, M.; Lindsey, J. S.; Bocian, D. F.; Holten, D. *J. Phys. Chem. B* **2004**, *108*, 8190–8200. (b) Taniguchi, M.; Kim, H. J.; Ra, D. Y.; Schwartz, J. K.; Kirmaier, C.; Hindin, E.; Diers, J. R.; Prathapan, S.; Bocian, D. F.; Holten, D.; Lindsey, J. S. *J. Org. Chem.* **2002**, *67*, 7329–7342. (c) Wiederrecht, G.P.; Svec, W. A.; Niemczyk, M. P.; Wasielewski, M. R. *J. Phys. Chem.* **1995**, *99*, 8918–8926. (d) Wiederrecht, G. P.; Niemczyk, M. P.; Svec, W. A.; Wasielewski, M. R. *J. Am. Chem. Soc.* **1996**, *118*, 81–88.

(10) (a) Ambroise, A.; Kirmaier, C.; Wagner, R. W.; Loewe, R. S.; Bocian, D. F.; Holten, D.; Lindsey, J. S. *J. Org. Chem.* **2002**, *67*, 3811–3826. (b) Loewe, R. S.; Lammi, R. K.; Diers, J. R.; Kirmaier, C.; Bocian, D. F.; Holten, D.; Lindsey, J. S. *J. Mater. Chem.* **2002**, *12*, 1530–1552. (c) Holten, D.; Bocian, D. F.; Lindsey, J. S. *Acc. Chem. Res.* **2002**, *35*, 57–69. (d) Tomizaki, K.; Loewe, R. S.; Kirmaier, C.; Schwartz, J. K.; Retsek, J. L.; Bocian, D. F.; Holten, D.; Lindsey, J. S. *J. Org. Chem.* **2002**, *67*, 6519–6534. (e) Yu, L.; Lindsey, J. S. *J. Org. Chem.* **2001**, *66*, 7402–7419. (f) Li, J.; Ambroise, A.; Yang, S. I.; Diers, J. R.; Seth, J.; Wack, C. R.; Bocian, D. F.; Holten, D.; Lindsey, J. S. *J. Am. Chem. Soc.* **1999**, *121*, 8927–8940. (g) Yang, S. I.; Seth, J.; Balasubramanian, T.; Kim, D.; Lindsey, J. S.; Holten, D.; Bocian, D. F. *J. Am. Chem. Soc.* **1999**, *121*, 4008–4018. (h) Susumu, K.; Therien, M. J. *J. Am. Chem. Soc.* **2002**, *124*, 8550–8552. (i) Shediac, R.; Gray, M. H. B.; Uyeda, H. T.; Johnson, R. C.; Hupp, J. T.; Angiolillo, P. J.; Therien, M. J. *J. Am. Chem. Soc.* **2000**, *122*, 7017–7033. (j) Kumble, R.; Palese, S.; Lin, V. S.-Y.; Therien, M. J.; Hochstrasser, R. M. *J. Am. Chem. Soc.* **1998**, *120*, 11489–11498.

(11) (a) Cho, H. S.; Rhee, H.; Song, J. K.; Min, C.-K.; Takase, M.; Aratani, N.; Cho, S.; Joo, T.; Kim, D. *J. Am. Chem. Soc.* **2003**, *125*, 5849–5860. (b) Mongin, O.; Hoyler, N.; Gossauer, A. *Eur. J. Org. Chem.* **2000**, *7*, 1193–1197. (c) Osuka, A.; Ikeda, M.; Shiratori, H.; Nishimura, Y.; Yamazaki, I. *J. Chem. Soc., Perkin Trans. 2* **1999**, 1019–1025.

(12) (a) Drain, C. M.; Batteas, J. D.; Flynn, G. W.; Milic, T.; Chi, N.; Yablon, D. G.; Sommers, H. *Proc. Natl. Acad. Sci. U.S.A.* **2002**, *99*, 6498–6502. (b) Milic, T. N.; Chi, N.; Yablon, D. G.; Flynn, G. W.; Batteas, J. D.; Drain, C. M. *Angew. Chem., Int. Ed.* **2002**, *41*, 2117–2119. (c) Shi, X.; Barkigia, K. M.; Fajer, J.; Drain, C. M. *J. Org. Chem.* **2001**, *66*, 6513–6522. (d) Drain, C. M.; Shi, X.; Milic, T.; Nifiatis, F. *Chem. Commun.* **2001**, *15*, 1418–1420. (e) Balaban, T. S.; Eichhofer, A.; Lehn, J.-M. *Eur. J. Org. Chem.* **2000**, *24*, 4047–4057.

(13) (a) Hunter, C. A.; Tregonning, R. *Tetrahedron* **2002**, *58*, 691–697. (b) Imahori, H.; Yamada, K.; Yoshizawa, E.; Hagiwara, K.; Okada, T.; Sakata, Y. *J. Porphyrins Phthalocyanines* **1997**, *1*, 55–66. (c) Armaroli, N.; Diederich, F.; Echegoyen, L.; Habicher, T.; Flamigni, L.; Marconi, G.; Nierengarten, J.-F. *New J. Chem.* **1999**, 77–83.

(14) (a) Hunter, C. A.; Sanders, J. K. M.; Beddard, G. S.; Evans, S. *J. Chem. Soc., Chem. Commun.* **1989**, 1765–1767. (b) Maiya, B. G.; Bampos, N.; Kumar, A. A.; Feeder, N.; Sanders, J. K. M. *New J. Chem.* **2001**, *25*, 797–800. (c) Mak, C. C.; Bampos, N.; Darling, S. L.; Montalti, M.; Prodi, L.; Sanders, J. K. M. *J. Org. Chem.* **2001**, *66*, 4476–4486.

(15) (a) Maeda, H.; Furuta, H. *Pure Appl. Chem.* **2006**, *78*, 29–44. (b) Harvey, J. D.; Ziegler, C. J. *J. Inorg. Biochem.* **2006**, *100*, 869–880. (c) Chmielewski, P. J.; Latos-Grazynski, L. *Coord. Chem. Rev.* **2005**, *249*, 2510–2533. (d) Srinivasan, A.; Furuta, H. *Acc. Chem. Res.* **2005**, *38*, 10–20.

(16) (a) Furuta, H.; Ishizuka, T.; Osuka, A.; Dejima, H.; Nakagawa, H.; Ishikawa, Y. *J. Am. Chem. Soc.* **2001**, *123*, 6207–6208. (b) Furuta, H.; Asano, T.; Ogawa, T. *J. Am. Chem. Soc.* **1994**, *116*, 767–8.

(17) Belair, J. P.; Ziegler, C. S.; Rajesh, C. S.; Modarelli, D. A. *J. Phys. Chem. A* **2002**, *106*, 6445–6451.

(18) (a) Gouterman, M. *J. Mol. Spectrosc.* **1961**, *6*, 138. (b) Gouterman, M. In *The Porphyrins*; Dolphin, D., Ed.; Academic Press: New York, 1978; Vol. III, pp 1−165. (c) Seybold, P. G.; Gouterman, M. *J. Mol. Spectrosc.* **1969**, *31*, 1–13.

(19) Alemán, E. A.; Rajesh, C. S.; Ziegler, C. S.; Modarelli, D. A. *J. Phys. Chem.* **2006**, *110*, 8605–8612.

(20) (a) Hanson, L. K. *Photochem. Photobiol.* **1988**, *47*, 903. (b) Zandler, M. E.; D'Souza, F. *J. Mol. Struct. Theochem.* **1997**, *401*, 301–314. (c) Waluk, J.; Muller, M.; Swiderek, P.; Kocher, M.; Vogel, E.; Hohlneicher, G.; Michl, J. *J. Am. Chem. Soc.* **1991**, *113*, 5511–5527.

(21) (a) Toyota, K.; Hasegawa, J.; Nakatsuji, H. *Chem. Phys. Lett.* **1996**, *250*, 437–42. (b) Tokita, Y.; Hasegawa, J.; Nakatsuji, H. *J. Phys. Chem. A* **1998**, *102*, 1843–1849. (c) Hasegawa, J.; Ozeki, Y.; Ohkawa, K.; Hada, M.; Nakatsuji, H. *J. Phys. Chem. B* **1998**, *102*, 1320–1326. (d) Nagashima, U.; Takada, T.; Ohno, K. *J. Chem. Phys.* **1986**, *85*, 4524–4529. (e) Wertsching, A. K.; Koch, A. S.; DiMagno, S. G. *J. Am. Chem. Soc.* **2001**, *123*, 3932–3939. (f) Helsinki, F. *Phys. Chem. Chem. Phys.* **2000**, *2*, 2275–2281.

(22) (a) Merchan, M.; Orti, E.; Roos, B. O. *Chem. Phys. Lett.* **1994**, *226*, 27–36. (b) Serrano-Andres, L.; Merchan, M.; Rubio, M.; Roos, B. O. *Chem. Phys. Lett.* **1998**, *295*, 195–203.

(23) (a) Sundholm, D. *Chem. Phys. Lett.* **1999**, *302*, 480–484. (b) Nguyen, K. A.; Day, P. N.; Pachter, R. *J. Phys. Chem. A* **2000**, *104*, 4748–4754. (c) Zhang, Y.-H.; Ruan, W-J.; Li, Z.-Y.; Wu, Y.; Zheng, J.-Y. *Chem. Phys.* **2005**, *315*, 201–213. (d) Nguyen, K. A.; Day, P. N.; Pachter, R. *J. Phys. Chem. A* **1999**, *103*, 9378–9382.

(24) Nooijen, M.; Bartlett, R. J. *J. Chem. Phys.* **1997**, *106*, 6449–6455.

(25) (a) Pachter, R.; Day, P. N.; Nguyen, K. A. *J. Phys. Chem. A* **1999**, *103*, 9378–9382. (b) Ghosh, A.; Parusel, A. B. J. *J. Phys. Chem. A* **2000**, *104*, 2504–2507.

(26) (a) Becke, A. D. *J. Chem. Phys.* **1983**, *98*, 5643. (b) Becke, A. D. *Phys. Rev. A* **1988**, *38*, 3098. (c) Lee, C.; Yang, W.; Parr, R. G. *Phys. Rev. B* **1988**, *37*, 785.

(27) *Gaussian 03, Revision C.02*. Frisch, M. J.; Trucks, G. W.; Schlegel, H. B.; Scuseria, G. E.; Robb, M. A.; Cheeseman, J. R.; Montgomery, J. A., Jr.; Vreven, T.; Kudin, K. N.; Burant, J. C.; Millam, J. M.; Iyengar, S. S.; Tomasi, J.; Barone, V.; Mennucci, B.; Cossi, M.; Scalmani, G.; Rega, N.; Petersson, G. A.; Nakatsuji, H.; Hada, M.; Ehara, M.; Toyota, K.; Fukuda, R.; Hasegawa, J.; Ishida, M.; Nakajima, T.; Honda, Y.; Kitao, O.; Nakai, H.; Klene, M.; Li, X.; Knox, J. E.; Hratchian, H. P.; Cross, J. B.; Bakken, V.; Adamo, C.; Jaramillo, J.; Gomperts, R.; Stratmann, R. E.; Yazyev, O.; Austin, A. J.; Cammi, R.; Pomelli, C.; Ochterski, J. W.; Ayala, P. Y.; Morokuma, K.; Voth, G. A.; Salvador, P.; Dannenberg, J. J.; Zakrzewski, V. G.; Dapprich, S.; Daniels, A. D.; Strain, M. C.; Farkas, O.; Malick, D. K.; Rabuck, A. D.; Raghavachari, K.; Foresman, J. B.; Ortiz, J. V.; Cui, Q.; Baboul, A. G.; Clifford, S.; Cioslowski, J.; Stefanov, B. B.; Liu, G.; Liashenko, A.; Piskorz, P.; Komaromi, I.; Martin, R. L.; Fox, D. J.; Keith, T.; Al-Laham, M. A.; Peng, C. Y.; Nanayakkara, A.; Challacombe, M.; Gill, P. M. W.; Johnson, B.; Chen, W.; Wong, M. W.; Gonzalez, C.; Pople, J. A.; Gaussian, Inc.: Wallingford CT, 2004.

(28) (a) Tomasi, J.; Persico, M. *Chem. Rev.* **1994**, *94*, 2027–2094. (b) Cossi, M.; Barone, V.; Cammi, R.; Tomasi, J. *Chem. Phys. Lett.* **1996**, *255*, 327–335. (c) Barone, V.; Cossi, M.; Tomasi, J. *J. Chem. Phys.* **1997**, *107*, 3210–3221. (d) Cossi, M.; Barone, V. *J. Chem. Phys.* **1998**, *109*, 6246–6254. (e) Barone, V.; Cossi, M.; Tomasi, J. *J. Comput. Chem.* **1998**, *19*, 404–417. (f) Cramer, C. J.; Truhlar, D. G. *Chem. Rev.* **1999**, *99*, 2161–2200.

(29) (a) Ahlrichs, R.; Bär, M.; Häser, M.; Horn, H.; Kölmel, C. *Chem. Phys. Lett.* **1989**, *162*, 165. (b) For the current version of TURBOMOLE,see: http://www.turbomole.de. (c) Treutler, O.; Ahlrichs, R. *J. Chem. Phys.* **1995**, *102*, 346.

(30) O'Boyle, N. M.; Vos, J. G. *GaussSum 1.0*; Dublin City University: Dublin, Ireland, 2005. Available from http://gausssum.sourceforge.net.

(31) (a) Ghosh, A.; Wondimagegn, T.; Nilsen, H. J. *J. Phys. Chem. B* **1998**, *102*, 10459–10467. (b) Zandler, M. E.; D'Souza, F. *J. Mol. Struct. (THEOCHEM)* **1997**, *401*, 301–314. (c) Szterenberg, L.; Latos-Grazyñski, L. *Inorg. Chem.* **1997**, *36*, 6287–6291.

(32) (a) Gouterman, M.; Wagnière, G.; Synder, L. C. *J. Mol. Spectrosc.* **1963**, *11*, 108. (b) Weiss, C.; Kobayashy, H.; Gouterman, M. *J. Mol. Spectrosc.* **1965**, *16*, 415. (c) Rimington, C.; Mason, S. F.; Kennard, O. *Spectrochim. Acta* **1958**, *12*, 65. (d) Anex, B. G.; Umans, R. S. *J. Am. Chem. Soc.* **1964**, *86*, 5026. (e) Edwards, L. E.; Dolphin, D. H.; Gouterman, M. *J. Mol. Spectrosc.* **1970**, *35*, 90. (f) Edwards, L.; Dolphin, D. H.; Gouterman, M.; Adler, A. D. *J. Mol. Spectrosc.* **1971**, *38*, 16. (g) Kim, B. F.; Bohandy, J. *J. Mol. Spectrosc.* **1978**, *73*, 332.

(33) (a) Parusel, A. B. J.; Grimme, S. *J. Porphyrins Phthalocyanines* **2001**, *5*, 225–232. (b) van Giesbergen, S. J. A.; Rosa, A.; Ricciardi, G.; Baerends, E. J. *J. Chem. Phys.* **1999**, *111*, 2499. (c) Sundholm, D. *Phys. Chem. Chem. Phys.* **2000**, *2*, 2275. (d) Hashimoto, T.; Choe, Y.-K.; Nakano, H.; Hirao, K. *J. Phys. Chem. A* **1999**, *103*, 1894. (e) Tokita, Y.; Hasegawa, J.; Nakatsuji, H. *J. Phys. Chem. A* **1998**, *102*, 1843. (f) Gwaltney, S. R.; Bartlett, R. J. *J. Chem. Phys.* **1998**, *108*, 6790. (g) Nooijen, M.; Bartlett, R. J. *J. Chem. Phys.* **1997**, *106*, 6449. (h) Serrano-Andrés, L.; Merchán, M.; Rubio, M.; Roos, B. O. *Chem. Phys. Lett.* **1998**, *295*, 195. (i) Kitao, O.; Ushiyama, H.; Mirua, N. *J. Chem. Phys.* **1999**, *110*, 2936.

(34) Zhang, Y.-H.; Ruan, W.-J.; Li, Z.-Y.; Wu, Y.; Zheng, J.-Y. *Chem. Phys.* **2005**, *315*, 201–213.

(35) Weiss, C. In *The Porphyrins*; Dolphin, D., Ed.; Academic Press: New York, 1978; Vol. III, pp 211−223.

(36) (a) *Density Functional Methods in Chemistry*; Labanowski, J., Ed.; Springer-Verlag: Heidelberg, Germany, 1991. (b) Parr, R. G.; Weitao, Y. *Density-Functional Theory in Atoms and Molecules*; Oxford University Press: New York, 1989. (c) Bauernschmitt, R. *Chem. Phys. Lett.* **1996**, *256*, 454. (d) Stratmann, E. R.; Scuseria, G. E.; Frisch, M. J. *J. Chem. Phys.* **1998**, *109*, 8218–8224. (e) Foresman, J. B.; Head-Gordon, M.; Pople, J. A.; Frisch, M. J. *J. Phys. Chem.* **1992**, *96*, 135–149.

(37) (a) Burdzinski, G.; Gustafson, T. L.; Hackett, J. C.; Hadad, C. M.; Platz, M. S. *J. Am. Chem. Soc.* **2005**, *127*, 13764–13765. (b) Burdzinski, G.; Hackett, J. C.; Wang, J.; Gustafson, T. L.; Hadad, C. M.; Platz, M. S. *J. Am. Chem. Soc.* **2006**, *128*, 13402–13411. (c) Wang, J.; Kubicki, J.; Burdzinski, G.; Hackett, J. C.; Gustafson, T. L.; Hadad, C. M.; Platz, M. S.

J. Org. Chem. **2007**, *72*, 7581–7586. (d) Vyas, S.; Onchoke, K. K.; Hadad, C. M.; Dutta, P. K. *J. Phys. Chem. A*,submitted.

(38) (a) Wiberg, K. B.; Hadad, C. M.; Breneman, C. M.; Laidig, K. E.; Murcko, M. A.; LePage, T. J. *Science* **1991**, *252*, 1266–1272. (b) Wiberg, K. B.; Hadad, C. M.; LePage, T. J.; Breneman, C. M.; Frisch, M. J. *J. Phys. Chem.* **1992**, *96*, 671–679. (c) Wiberg, K. B.; Hadad, C. M.; Foresman, J. B.; Chupka, W. A. *J. Phys. Chem.* **1992**, *96*, 10756–10768. (d) Hadad, C. M.; Foresman, J. B.; Wiberg, K. B. *J. Phys. Chem.* **1993**, *97*, 4293–4312. (e) Wiberg, K. B.; Hadad, C. M.; Ellison, G. B.; Foresman, J. B. *J. Phys. Chem.* **1993**, *97*, 13586–13597.

JP802094R